Supporting Information

In Situ Spectroelectrochemical Probing of CO Redox Landscape on Copper Single-Crystal Surfaces

Feng Shao,[a, b, c *] Jun Kit Wong,[c] Qi Hang Low,[c, d] Marcella Iannuzzi,[e] Jingguo Li,[e *] Jinggang Lan[e *]

[a] *State Key Laboratory of Materials-Oriented Chemical Engineering, College of Chemical Engineering, Nanjing Tech University, Nanjing, 211816, China*

[b] *Department of Physics and Astronomy, National Graphene Institute, University of Manchester, Manchester, M13 9PL, UK;*

[c] *Department of Chemistry, Faculty of Science, National University of Singapore, Singapore 117543, Singapore;*

[d] *Solar Energy Research Institute of Singapore, National University of Singapore, Singapore 117574, Singapore; and*

[e] *Department of Chemistry, University of Zurich, Zurich 8057, Switzerland*

*Corresponding Authors: feng-shao@hotmail.com; jingguo.li@ kemi.uu.se; jinggang.lan@epfl.ch.

Current address: *Dr. J. Li: Department of Chemistry − Ångström Laboratory, Uppsala University, Uppsala, 75120, Box 523, Sweden; Dr. J. Lan: Chaire de Simulation à l'Echelle Atomique (CSEA), Ecole Polytechnique Fédérale de Lausanne (EPFL), Lausanne, CH-1015 , Switzerland.*

Table of contents

1. Supporting Figures

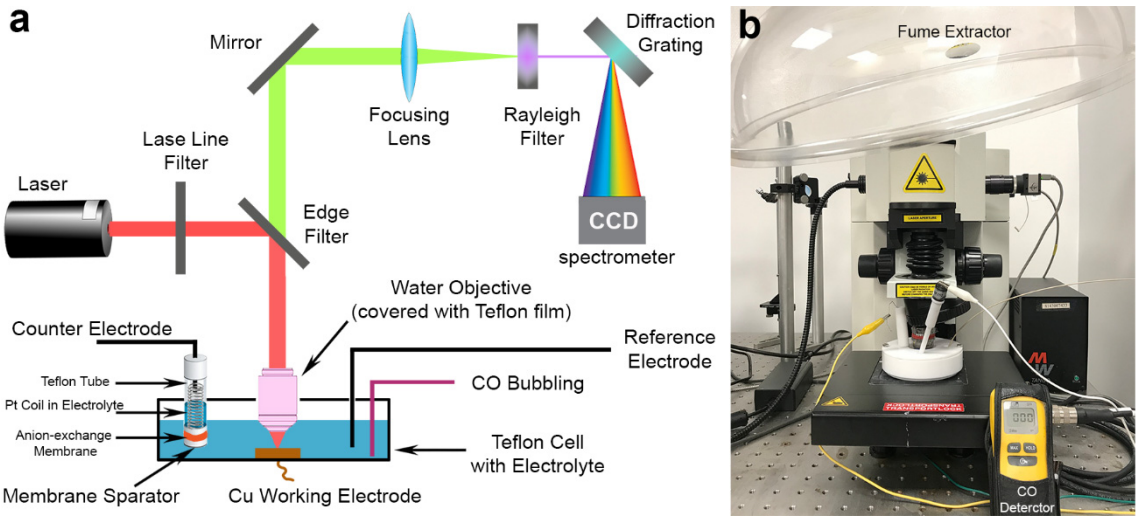

Figure S1 | (a) Schematic diagram and (b) photograph of the electrochemical/Raman spectroscopy setup. For security reasons, the fume extractor remains working during the CO bubbling, and the environmental CO concentration is continuously monitored by a CO detector.

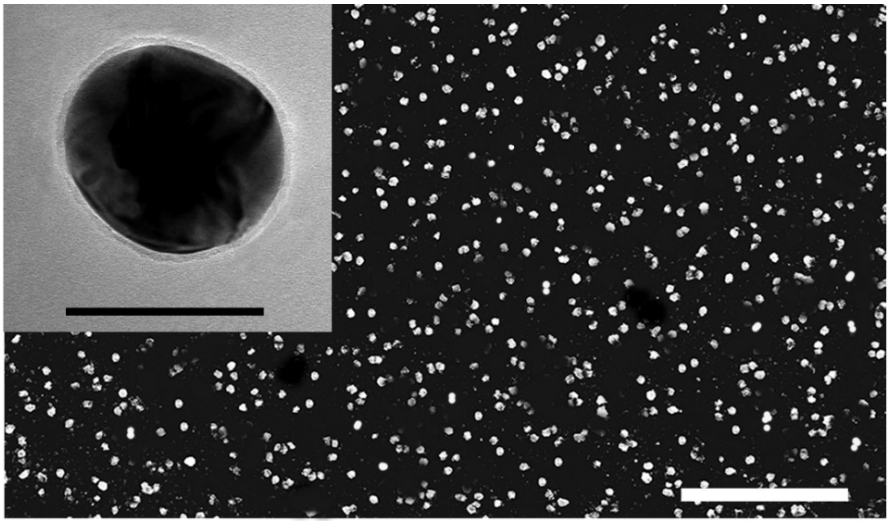

Figure S2 | Scanning electron microscope (SEM) image of a Cu(100) surface modified by Au@SiO_2 SHINs (scale bar: 2 μm). Insert: transmission electron microscope (TEM) image of a typical Au@SiO_2 nanoparticle (scale bar: 50 nm).

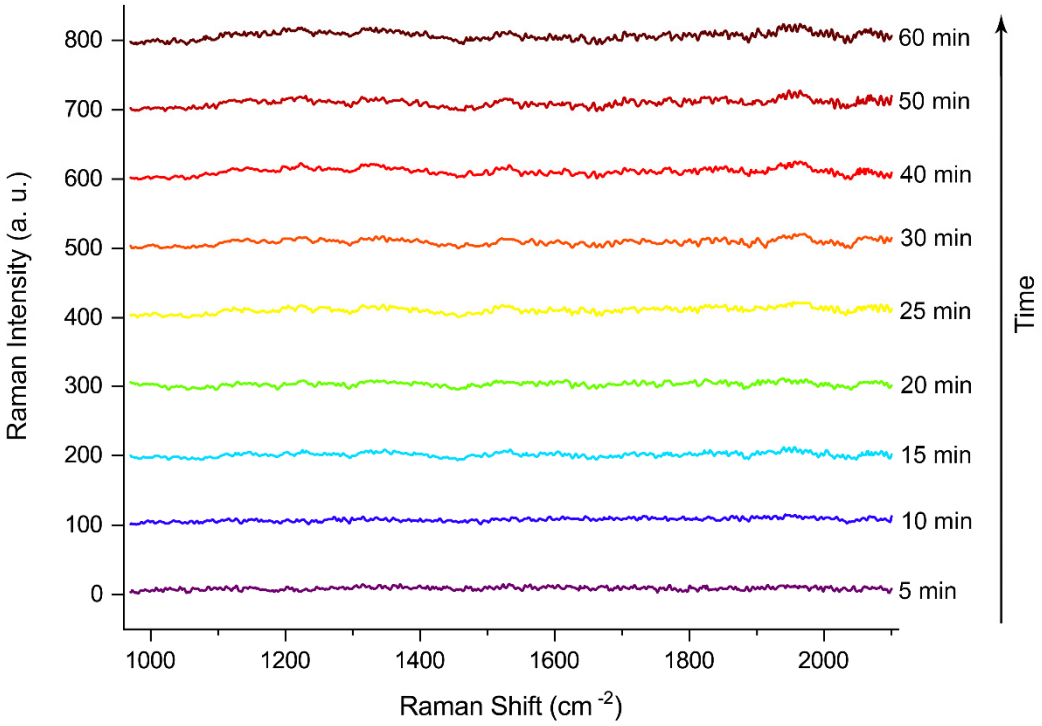

Figure S3 | The pinhole test of Au@SiO_2 SHINs in 0.1 M CsOH mixed with different time. Au@SiO_2 SHINs were deposited on Si substrates. Probe solution: 20 uL 0.1 M CsOH + 5 uL pyridine. The spectra were collected at open circuit potential (OCP).(1) a.u. arbitrary units.

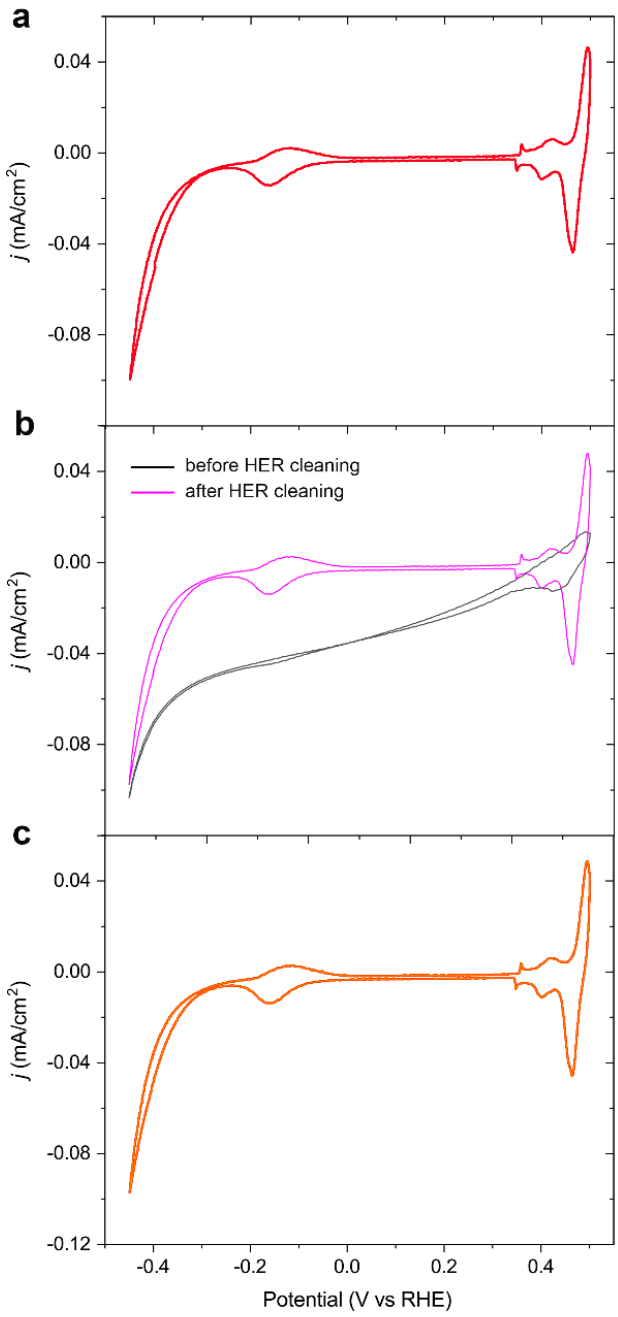

Figure S4 | (a) CVs results of Cu(100) single-crystal electrodes without a coating of Au@SiO_2 SHINs before the CORR. (b) CVs results of Cu(100) single-crystal electrodes with a coating of Au@SiO_2 SHINs before and after the HER cleaning. (d) CVs results of Cu(100) single-crystal electrodes with a coating of Au@SiO_2 SHINs after the CORR. All potentials are referenced to the reversible hydrogen electrode (RHE).

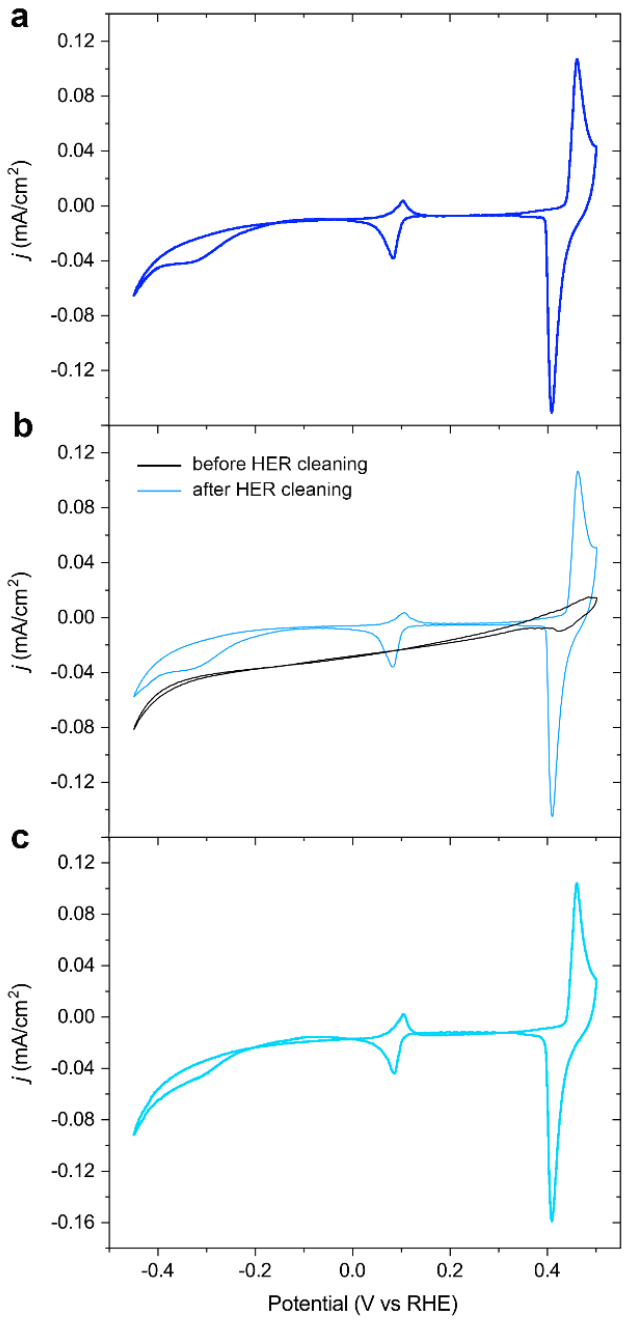

Figure S5 | (a) CVs results of Cu(111) single-crystal electrodes without a coating of Au@SiO_2 SHINs before the CORR. (b) CVs results of Cu(111) single-crystal electrodes with a coating of Au@SiO_2 SHINs before and after the HER cleaning. (d) CVs results of Cu(111) single-crystal electrodes with a coating of Au@SiO_2 SHINs after the CORR. All potentials are referenced to the reversible hydrogen electrode (RHE).

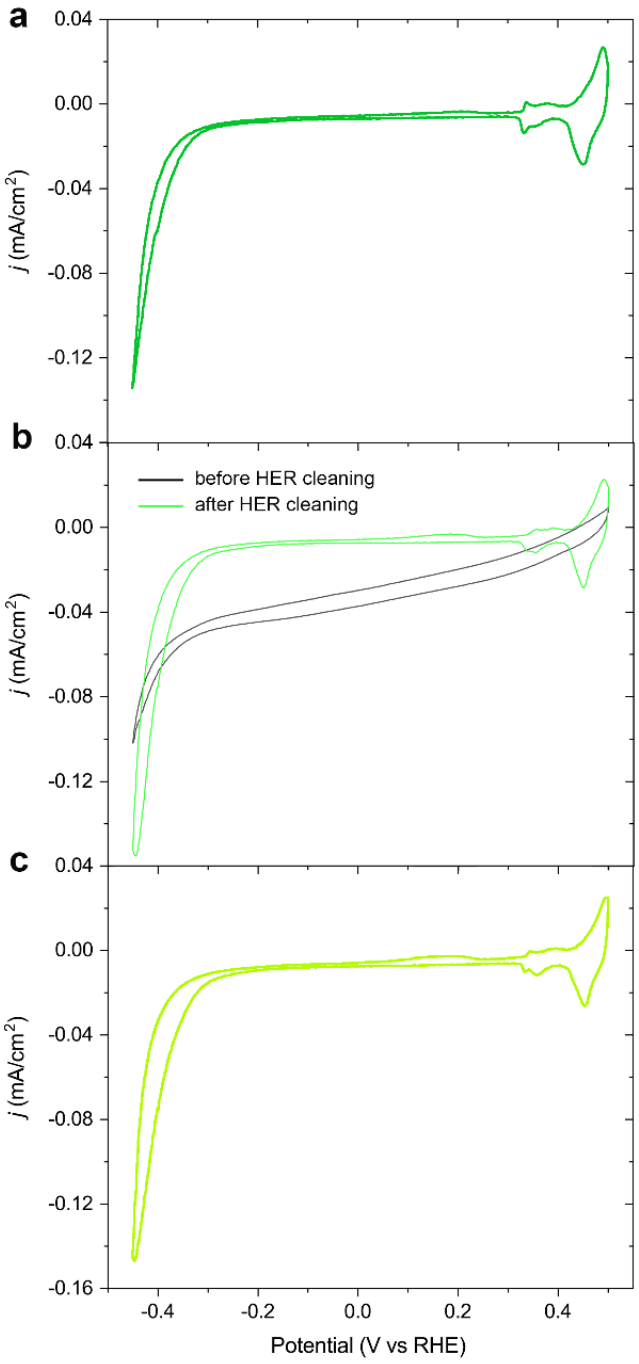

Figure S6 | (a) CVs results of Cu(110) single-crystal electrodes without a coating of Au@SiO_2 SHINs before the CORR. (b) CVs results of Cu(110) single-crystal electrodes with a coating of Au@SiO_2 SHINs before and after the HER cleaning. (d) CVs results of Cu(110) single-crystal electrodes with a coating of Au@SiO_2 SHINs after the CORR. All potentials are referenced to the reversible hydrogen electrode (RHE).

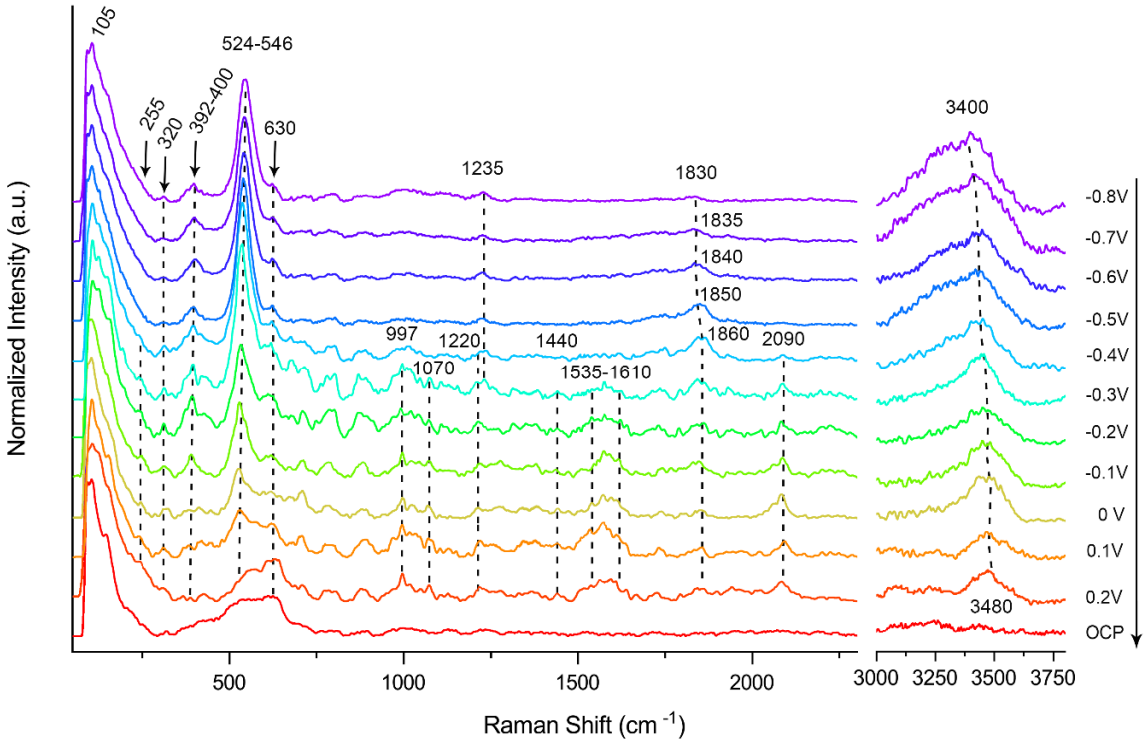

Figure S7 | Normalized EC-SHINERS spectra (40-4000 cm^{-1}) recorded on Cu(100) in the ^{12}CO-saturated CsOH (0.1M) solution at different applied potentials (vs. RHE, OCP: open circuit potential). The anodic back scan starts from -0.8 to +0.2 V. The low-frequency band at 105 cm^{-1} is characteristic of the optical fibers used in our spectrometer, and is used as a normalization reference and internal standard to compensate for differences in signal intensities due to laser alignment. a.u. arbitrary units.

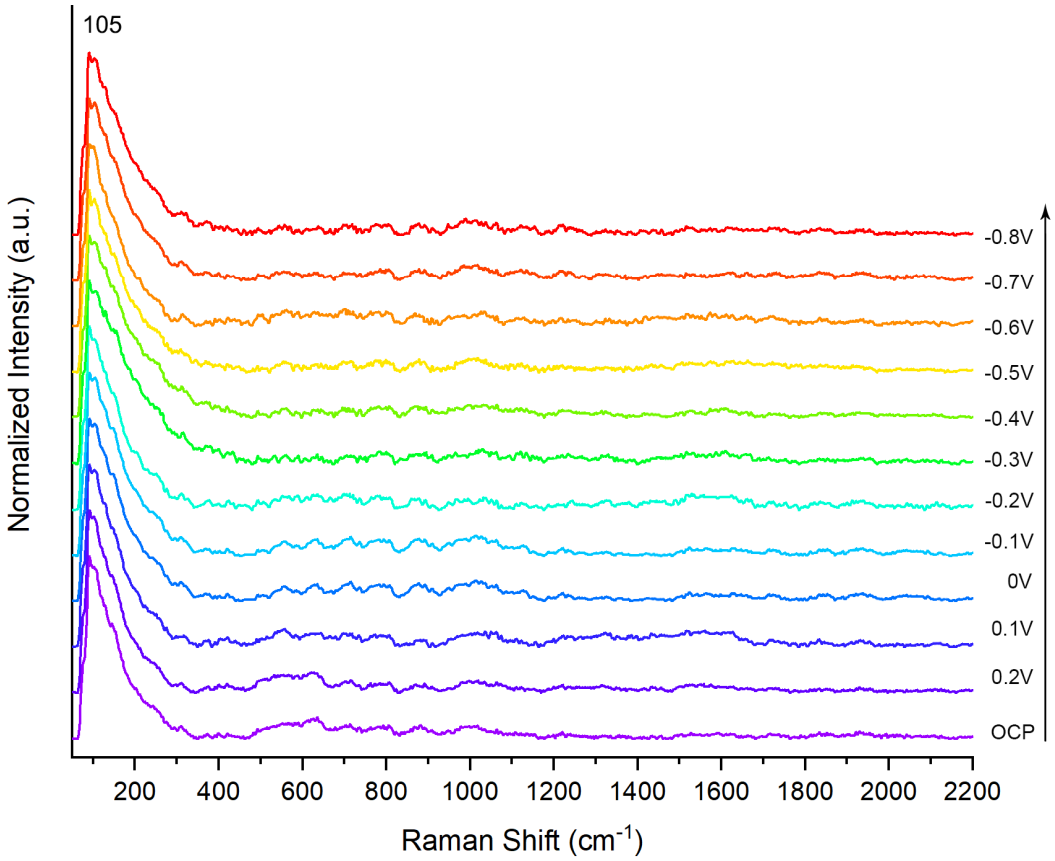

Figure S8 | Normalized Raman spectra recorded from Cu(100) in the CO-saturated CsOH (0.1 M) solution at different applied potentials (vs. RHE, OCP: open circuit potential). Without SHINs to provide sufficient enhancement, no significant Raman features can be recorded from the interesting Raman ranges on Cu(100). The low-frequency band at 105 cm^{-1} is characteristic of the optical fibers used in our spectrometer, and is used as a normalization reference and internal standard to compensate for differences in signal intensities due to laser alignment. a.u. arbitrary units.

Table S1 | Assignments of vibrational frequencies for oxygen-containing species during the CORR in alkaline electrolytes (pH=13) on Cu surfaces.

Assignments	Raman Shifts (cm^{-1})								References
Cu_2O									
Powder	147	216			412	514	635		(1)
Anodic film						525	625		(2)
Deposited film		218				523	623		(3)
Nanocrystal	150	220			415	520	630		(4)
CuO									
Powder			288	337			638		(1)
Deposited film			298	347			591		(3)
Tenorite			296	347			631		(5)
Nanorod			273	321			606		(6)
Foil			287	329			619		(7)
$Cu(OH)_2$									
Powder			288	337	450	489			(1)
Anodic film					460				(2)
Deposited film						490			(3)
Anodic film			292			488			(8)
$(Cu_2O)_{surf}$	143	222			450	525	627		(1)
	146	219			412	528	619		(9)
$CuO_x/(OH)_y$				395		530			(10)
Cu-OH_{ad}						520-544			This work
					453	525-535		660-710	(1)
					460			800	(2)
								709	(10)
				431	450	527			(11)
						527			(12)
					460	520		698	(13) (14)
Cu-OD_{ad}						516-538			This work
						497		640	(1)
								725	(13)
Cu-O_{ad}				320	393-400		630		This work
							570-633		(1)
							625		(2)
							620		(10)
				320	380				(14)
Cu-CO_{ad}			255				2060	2090	This work
					1800-1900		2050-2100		(10)
			275	360	502		2050-2070		(14)
			280	365			1900-2100		(15)
				340-350			2060-2074		(16)
			280	360			1980-2100		(17)

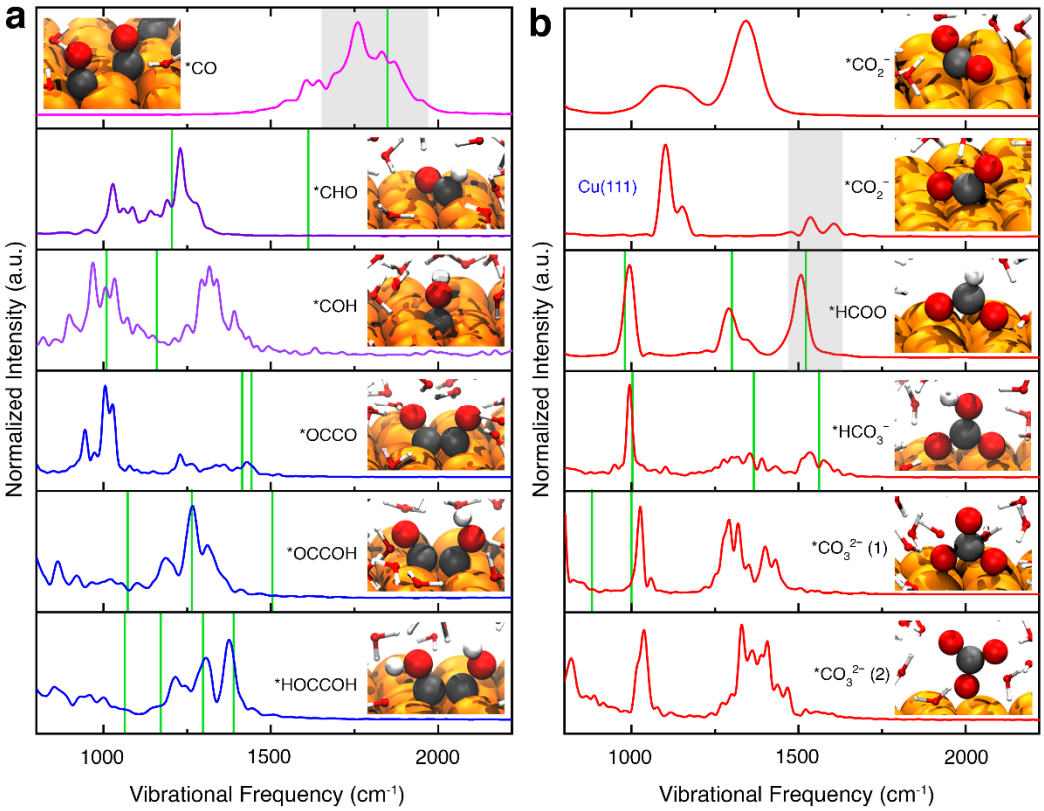

Figure S9 | The calculated VDOSs of intermediates from AIMD simulations (in blue and red curves) and the static frequency predictions from DFT calculations (in green lines) during the CORR and CORR. Assignments of these typical frequencies are listed in Tables **S2** and **S3**. a.u. arbitrary units.

Table S2 | Assignments of vibrational frequencies for surface adsorbed species during the CORR in alkaline electrolytes (pH=13) on Cu (100). [a] Since the OCCO structure is unstable on the neutral Cu surface, the Cu(100) slab was charged with one extra electron while the compensation charge was included with one Cs ion near the surface. H-bonding indicates that the surface species show a significant hydrogen bonding effect with solvent water.

Assignments	Frequencies (cm^{-1})			Literatures
	Experimental	Calculated		
*CO		AIMD	DFT	
C≡O stretching	2120; 2090; 2060			This work (18-23)
C=O stretching	1830-1864 (1838-1867)	1870-1760	1848	This work (24)
*CHO				
CHO in-plane bending	1235	1230 (H-bonding)	1205 (1235)	This work (25)
C-H in-plane bending		1030 (H-bonding)		This work
*COH				
C-OH bending		1320 (H-bonding)	1163 (1160)	This work (25)
C-OH stretching		1030 (H-bonding)	1014 (1020)	This work (25)
C-O stretching		970 (H-bonding)		This work
*OCCO[a]				
C=O stretching	(1550-1562)		1498, 1553	(26)
asymmetry stretching		1430	1438 (1486)	This work (25)
symmetry stretching			1412	This work
asymmetry stretching		1235 (1229) (H-bonding)		This work (27)
symmetry stretching		1005 (1039) (H-bonding)		This work (27)
C=O bending		945 (H-bonding)		This work
*OCCOH				
C-O stretching	(1584)		(1576)	(25)
C=O stretching			1508	This work
C=O stretching		1310 (H-bonding)		This work
C-O-H stretching	(1191)	1265 (1231)	1265 (1235, 1242)	This work (25-27)
C-OH stretching		1185 (H-bonding)	1077	This work
*OCCHO				
C=O stretching			(1313, 1376)	(25, 26)
C-O stretching			(1200, 1206)	(25, 26)
*HOCCOH				
C=C stretching	1370	1375	1383 (1397)	This work (25)
C-OH bending		1310 (1324)	1300 (1229)	This work (25, 27)
C-OH bending	1220	1215 (1187)	1175	This work (27)
*C=C=O				
asymmetry stretching	1960	1987 (2078) (H-bonding)	2070	This work (27)
symmetry stretching		1200 (1211)	1206	This work (27)
C=C=O *bending*		556	605	This work

Table S3 | Assignments of vibrational frequencies for surface adsorbed species during the COOR in alkaline electrolytes (pH=13) on Cu (100) and Cu(111).

Assignments	Frequencies (cm^{-1})			Literatures
	Experimental	Calculated		
*CO_2^- on Cu(100)		AIMD	DFT	
in-plane CO_2 bending		725		This work
symmetry C-O stretching		1105		This work
asymmetry C-O stretching	(1330, 1325)	1345 (1365)		This work (28) (16)
*CO_2^- on Cu(111)				
in-plane CO_2 bending	(700)	680	(733)	This work (16)
symmetry C-O stretching	(1330)	1103	(967)	This work (16)
asymmetry C-O stretching	1535-1610 (1543)	1535-1604	(1503)	This work (16)
*HCOO				
O-C-O bending		994	990	This work
symmetry O-C-O stretching		1290	1308	This work
asymmetry O-C-O stretching		1506	1528	This work
*HCO_3^-				
C-O stretching	997 (1015)	995	1002	This work (17, 29)
C-O stretching	(1363, 1360) (1345, 1362)	1353	1365	This work (29, 30) (14, 31)
asymmetry O-C-O stretching	1535-1610	1535	1553	This work
*CO_3^{2-} (1)				
symmetry O-C-O stretching			914	This work
asymmetry O-C-O stretching	997 (990)	1025	1000	This work (32)
C-O stretching		1293		This work
C-O stretching		1320		This work
C-O stretching	(1390, 1395)	1400 (1400)		This work (28) (30, 33)
C-O stretching	1440 (1430)	1432		This work (16)
*CO_3^{2-} (2)				
C-O stretching	1070 (1070, 1065) (1060)	1040 (1034)		This work (28) (14, 29) (34)
C-O stretching	(1344)	1330		This work (14)
C-O stretching	(1390, 1395)	1407 (1400)		This work (28) (30, 33)

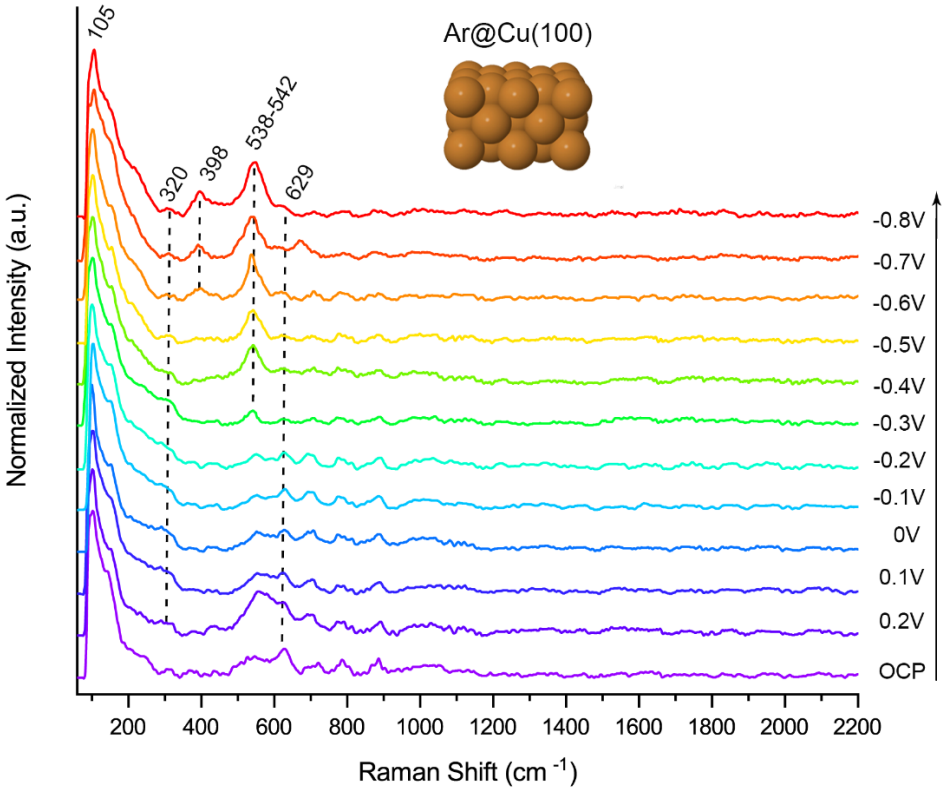

Figure S10 | Normalized EC-SHINERS spectra recorded from Cu(100) in the Ar-saturated CsOH (0.1 M) solution at different applied potentials (vs. RHE, OCP: open circuit potential). Assignments of vibrational frequencies for O-containing species can be found in Table S1. The low-frequency band at 105 cm^{-1} is characteristic of the optical fibers used in our spectrometer, and is used as a normalization reference and internal standard to compensate for differences in signal intensities due to laser alignment. All potentials are referenced to the reversible hydrogen electrode (RHE). a.u. arbitrary units.

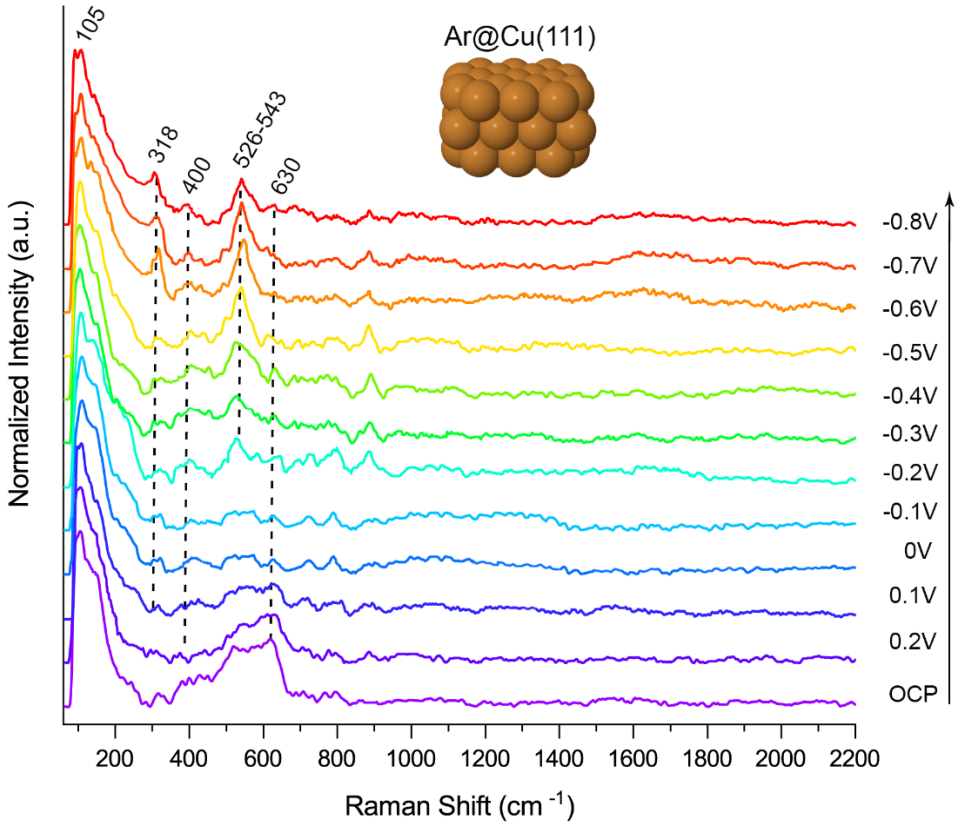

Figure S11 | Normalized EC-SHINERS spectra recorded from Cu(111) in the Ar-saturated CsOH (0.1 M) solution at different applied potentials (vs. RHE, OCP: open circuit potential). Assignments of vibrational frequencies for O-containing species can be found in Table S1. The low-frequency band at 105 cm^{-1} is characteristic of the optical fibers used in our spectrometer, and is used as a normalization reference and internal standard to compensate for differences in signal intensities due to laser alignment. All potentials are referenced to the reversible hydrogen electrode (RHE). a.u. arbitrary units.

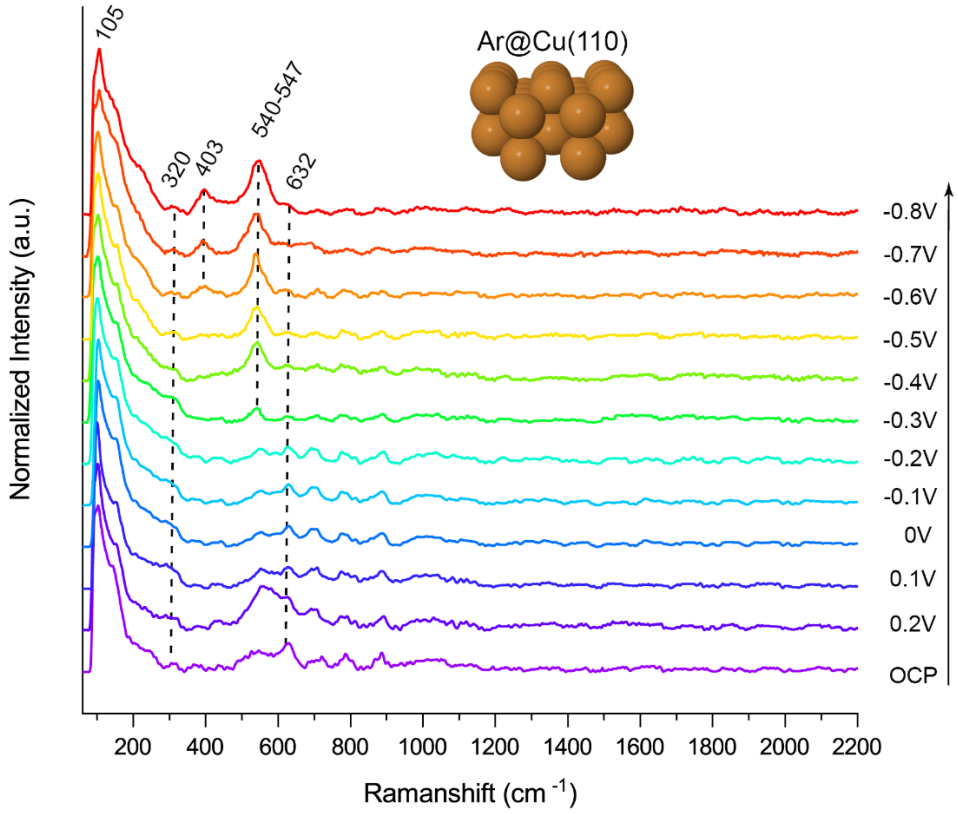

Figure S12 | Normalized EC-SHINERS spectra recorded from Cu(110) in the Ar-saturated CsOH (0.1 M) solution at different applied potentials (vs. RHE, OCP: open circuit potential). Assignments of vibrational frequencies for O-containing species can be found in Table S1. The low-frequency band at 105 cm^{-1} is characteristic of the optical fibers used in our spectrometer, and is used as a normalization reference and internal standard to compensate for differences in signal intensities due to laser alignment. All potentials are referenced to the reversible hydrogen electrode (RHE). a.u. arbitrary units.

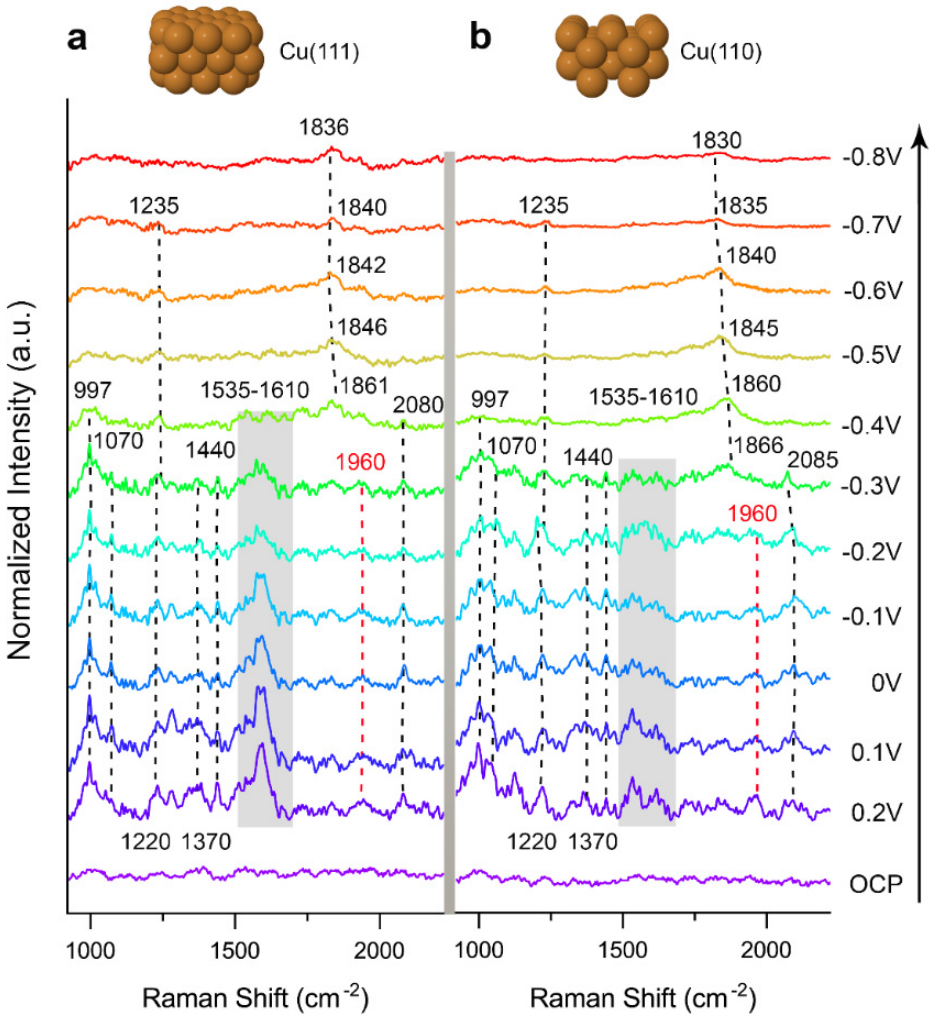

Figure S13 | Normalized EC-SHINERS recorded from (a) Cu(111) and (b) Cu(110) in 0.1 M ^{12}CO-saturated CsOH solutions (pH=13, OCP: open circuit potential). Assignments of these typical frequencies are listed in Tables **S1**and **S2**. The 1960 cm^{-1} band can be assigned to the asymmetric C=C=O stretching modes of a surface ketene (*C=C=O) species according to the calculated VDOSs (at 1987 cm^{-1}, Fig. S20) (35, 36). The low-frequency band at 105 cm^{-1} is characteristic of the optical fibers used in our spectrometer, and is used as a normalization reference and internal standard to compensate for differences in signal intensities due to laser alignment. All potentials are referenced to the reversible hydrogen electrode (RHE). a.u. arbitrary units.

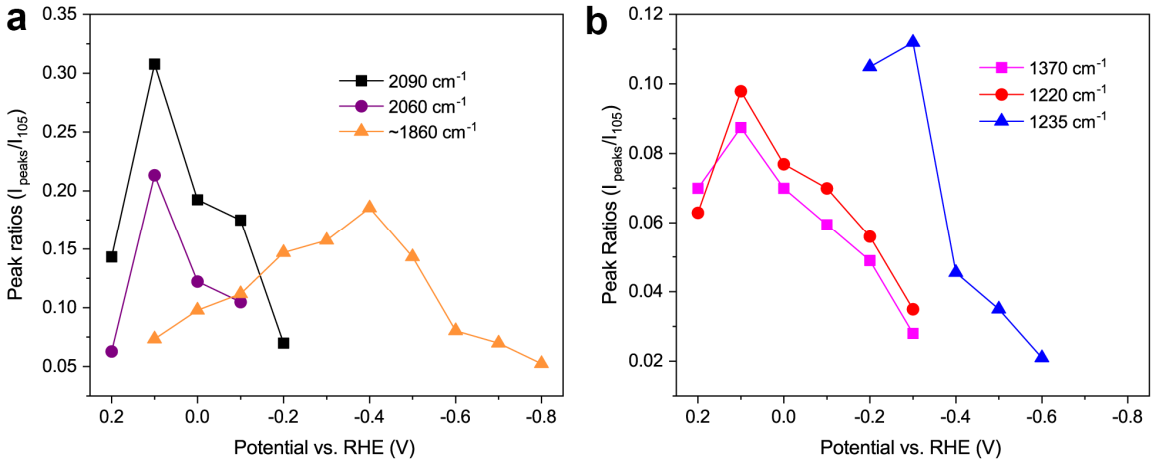

Figure S14 | Potential dependence of the peak ratios (I_{peak}/I_{105}) of (a) *CO_{atop} (2090 and 2060 cm^{-1}), *CO_{bridge} (~1860 cm^{-1}), and (b) *HOCCOH (1370 and 1220 cm^{-1}) and *CHO (1235 cm^{-1}) during the CORR on Cu(100). This prototype data was taken from Figure 2a. The low-frequency band at 105 cm^{-1} is characteristic of the optical fibers used in our spectrometer and is used as a normalization reference and internal standard to compensate for differences in signal intensities due to laser alignment. All potentials are referenced to the reversible hydrogen electrode (RHE). Here we try to provide insights into the change trends of these specific Raman signals during the CORR under different conditions. This attempt is based on the following facts: (i) except the applied potentials, other experimental parameters (Cu facets, electrolytes, CO bubble rates, laser wavelengths, incident power, acquisition time, etc.) have been kept constant; (ii) the data recorded (ca. 10 spectra) across different locations on the Cu surfaces and has been averaged for further presentation; (iii) all the averaged spectra have been normalized to the intensity of the highest 105 cm^{-1} bands as an internal standard. Accordingly, these averaged spectra with the normalized intensity ratio (I_{peak}/I_{105}) can help us to find out the general change trend of surface species along with the applied potentials, as similarly reported by other groups. (37-39)

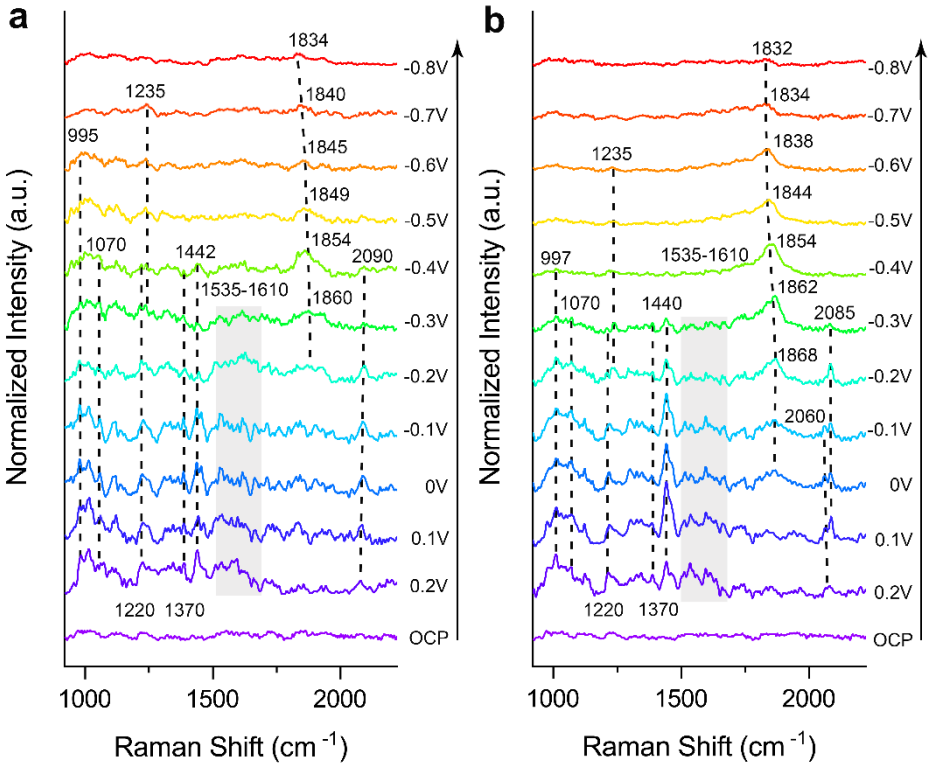

Figure S15 | Normalized EC-SHINERS recorded from Cu(100) in 0.1 M ^{12}CO-saturated (a) LiOH (pH=12.3) and (b) KOH solutions (pH=13.0, OCP: open circuit potential). Assignments of these typical frequencies are listed in Tables **S2** and **S3**. The low-frequency band at 105 cm^{-1} is characteristic of the optical fibers used in our spectrometer, and is used as a normalization reference and internal standard to compensate for differences in signal intensities due to laser alignment. All potentials are referenced to the reversible hydrogen electrode (RHE). a.u. arbitrary units.

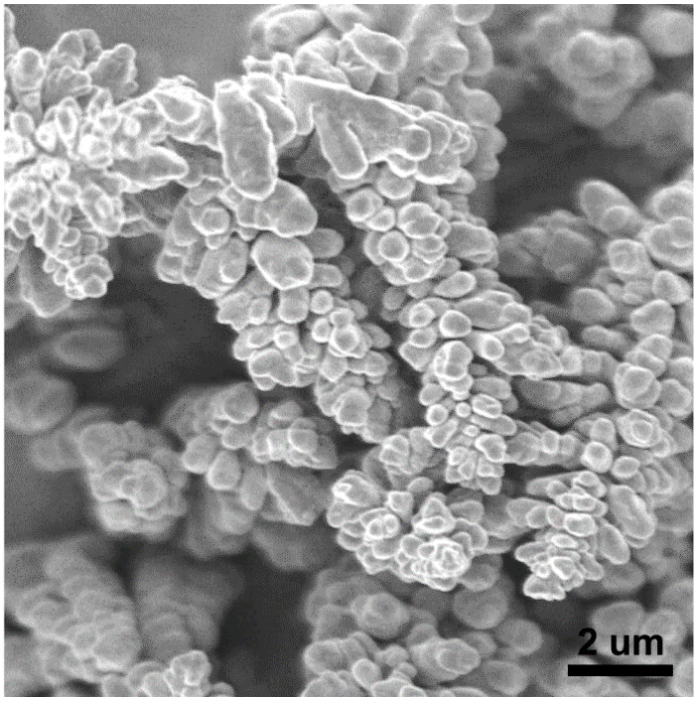

Figure S16 | SEM images of the roughened polycrystalline Cu electrode.

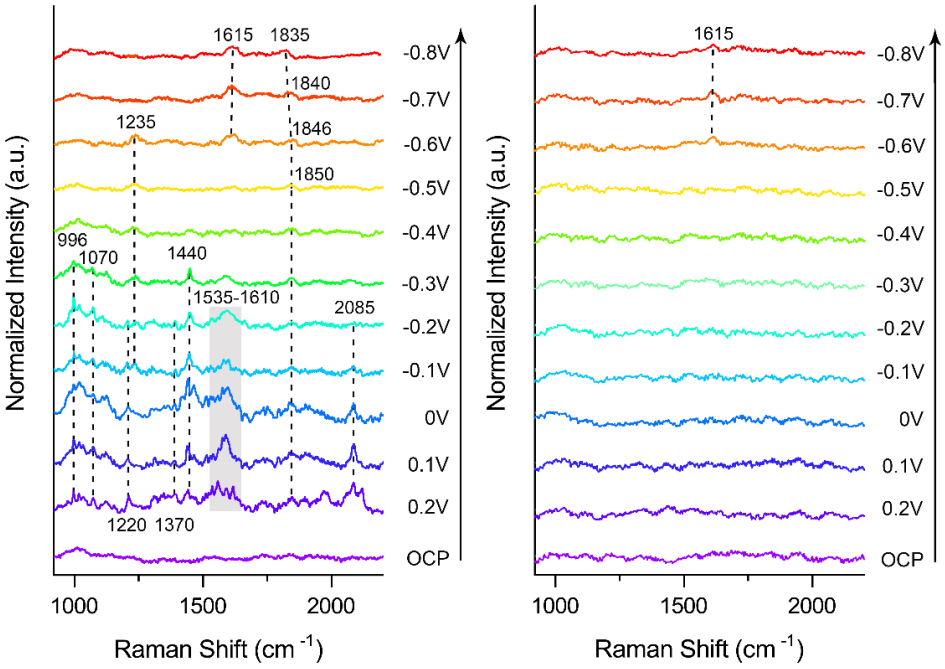

Figure S17 | Normalized EC-SHINERS recorded from the roughened polycrystalline Cu electrode in 0.1 M (a) ^{12}CO- and (b) Ar-saturated CsOH solutions (pH=13, OCP: open circuit potential). Assignments of these typical frequencies are listed in Tables **S1** and **S2**. The Raman peak at 1615 cm^{-1} can be assigned to the H–O–H bending mode of interfacial water at the Cu(100) surface.(40) The low-frequency band at 105 cm^{-1} is characteristic of the optical fibers used in our spectrometer and is used as a normalization reference and internal standard to compensate for differences in signal intensities due to laser alignment. All potentials are referenced to the reversible hydrogen electrode (RHE). a.u. arbitrary units.

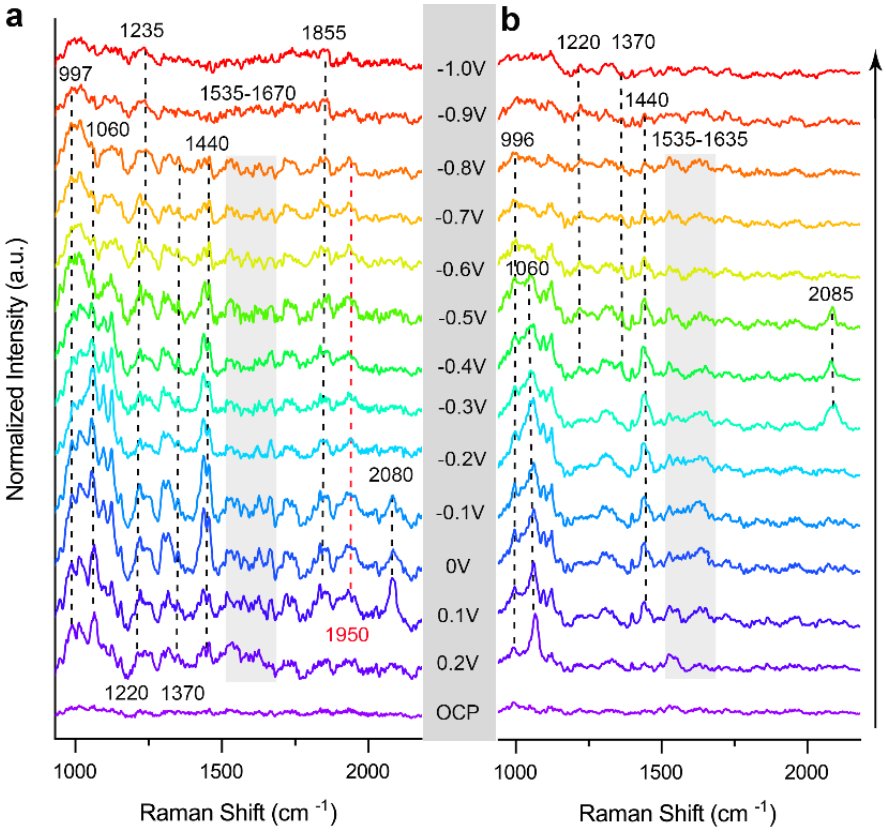

Figure S18 | Normalized EC-SHINERS recorded from Cu(100) in 0.1 M (a) ^{12}CO- and (b) Ar-saturated $CsHCO_3$ solutions (pH=9.0, OCP: open circuit potential). Assignments of these typical frequencies are listed in Tables **S1** and **S2**. All potentials are referenced to the reversible hydrogen electrode (RHE). A new CO band at 2085 cm^{-1} appears under potentials of -0.3V to -0.5V in the Ar-saturated $CsHCO_3$ solution (b), demonstrating that bicarbonate anions play a critical role in the CO_2RR and they can directly adsorb onto Cu surfaces to generate initial CO products.(41) At more negative potentials, the CORR occurs on Cu(100) since its typical intermediates are visible in the spectra at 1220, 1235, and 1370 cm^{-1} under such conditions (see Tables **S2** and **S3**). The 1950 cm^{-1} band can be assigned to the asymmetric C=C=O stretching modes of a surface ketene (*C=C=O) species according to the calculated VDOSs (at 1987 cm^{-1}, Fig. S20)(35, 36). The low-frequency band at 105 cm^{-1} is characteristic of the optical fibers used in our spectrometer, and is used as a normalization reference and internal standard to compensate for differences in signal intensities due to laser alignment. a.u. arbitrary units.

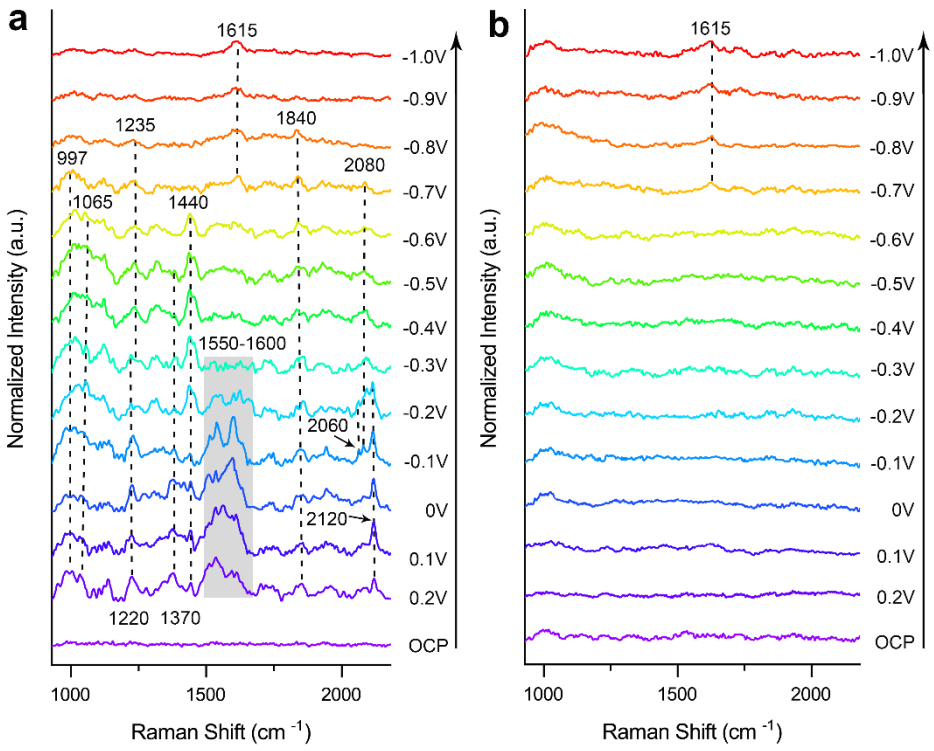

Figure S19 | Normalized EC-SHINERS recorded from Cu(100) in 0.1 M (a) ^{12}CO- and (b) Ar-saturated CsCl solutions (pH=7.0, OCP: open circuit potential). Assignments of these typical frequencies are listed in Tables **S1** and **S2**. The Raman peak at 1615 cm^{-1} can be assigned to the H–O–H bending mode of interfacial water at the Cu(100) surface.(40) The low-frequency band at 105 cm^{-1} is characteristic of the optical fibers used in our spectrometer, and is used as a normalization reference and internal standard to compensate for differences in signal intensities due to laser alignment. All potentials are referenced to the reversible hydrogen electrode (RHE). a.u. arbitrary units.

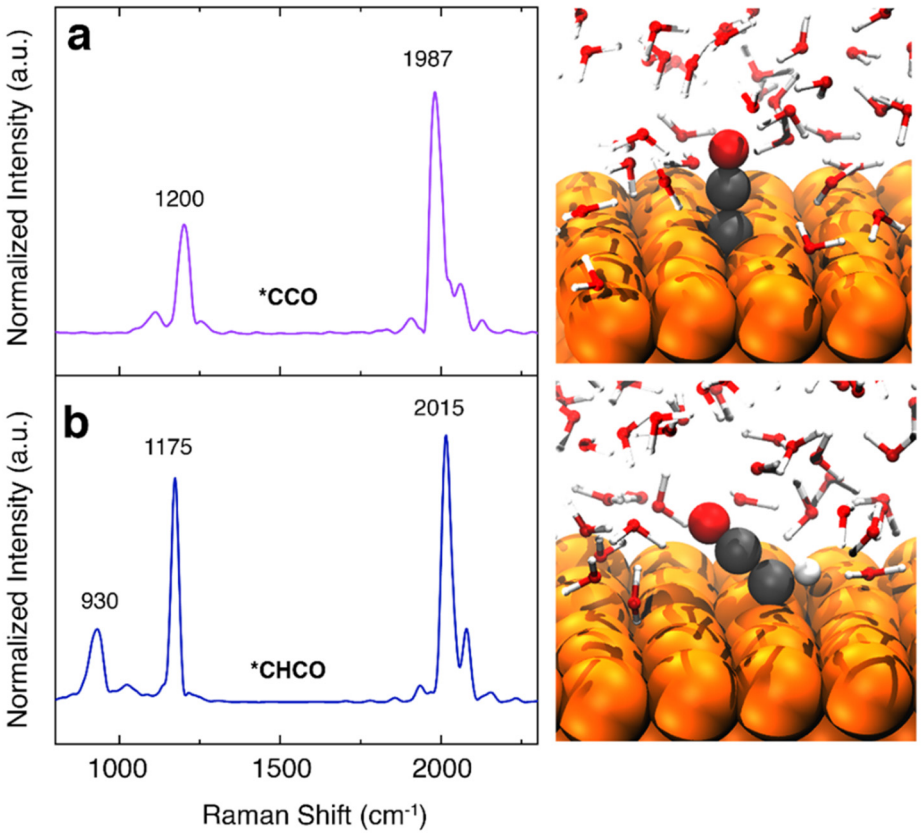

Figure S20 | VDOSs of (a) *CCO and (b) *CHCO as obtained from AIMD and representative snapshots of typical reaction intermediates during the CORR on Cu(100). The Cu, C, O, and H atoms are presented in orange, black, red, and white colours, respectively. a.u. arbitrary units.

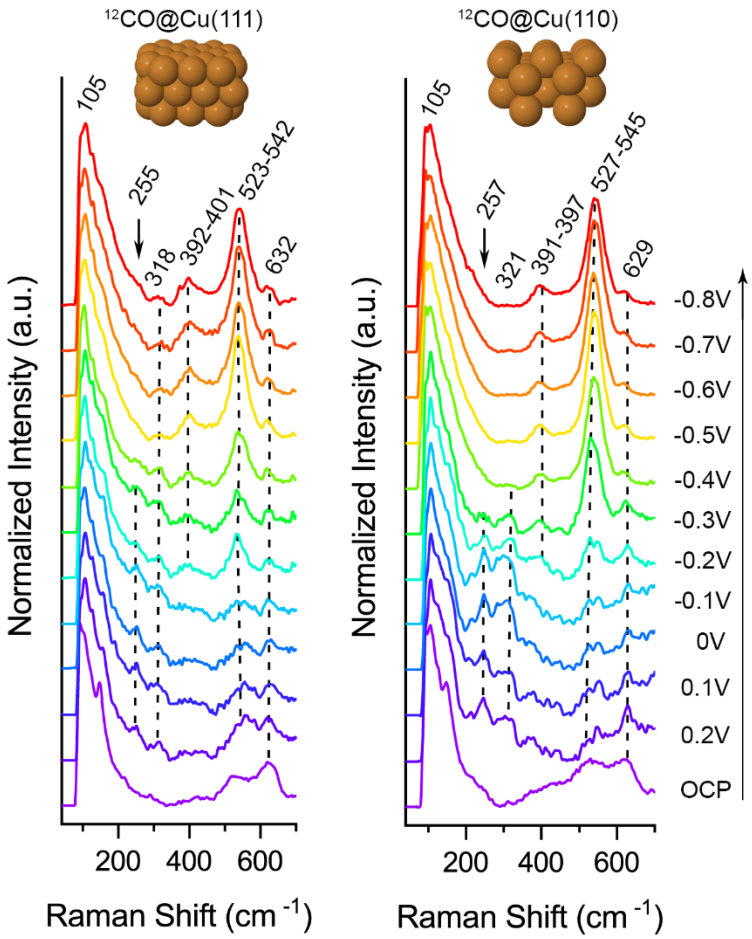

Figure S21 | Normalized EC-SHINERS spectra recorded from various Cu surfaces in the ^{12}CO-saturated CsOH (0.1 M) solution at different applied potentials (OCP: open circuit potential). The low-frequency band at 105 cm^{-1} is characteristic of the optical fibers used in our spectrometer, and is used as a normalization reference and internal standard to compensate for differences in signal intensities due to laser alignment. All potentials are referenced to the reversible hydrogen electrode (RHE). a.u. arbitrary units.

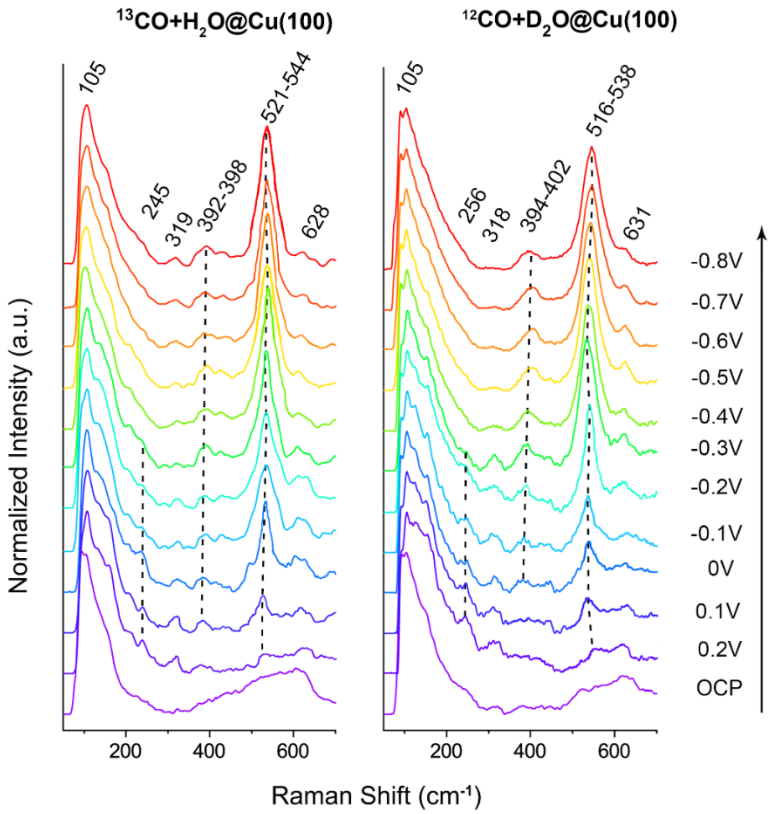

Figure S22 | Normalized EC-SHINERS spectra recorded from Cu(100) in the ^{13}CO-saturated CsOH (0.1 M) and ^{12}CO-saturated CsOD (0.1 M) solutions at different applied potentials (OCP: open circuit potential). The low-frequency band at 105 cm^{-1} is characteristic of the optical fibers used in our spectrometer, and is used as a normalization reference and internal standard to compensate for differences in signal intensities due to laser alignment. All potentials are referenced to the reversible hydrogen electrode (RHE). Compared to Fig. 2a, the small peak around 255 cm^{-1} was red-shifted to 245 cm^{-1} (Fig. S22) in the ^{13}CO-saturated CsOH solution, while kept constant (256 cm^{-1}, Fig. S22) in the ^{12}CO-saturated CsOD solution, indicating it originated from C-bound species. This mode is calculated to be a bending mode of an adsorbed CO on Cu hollow sites. a.u. arbitrary units.

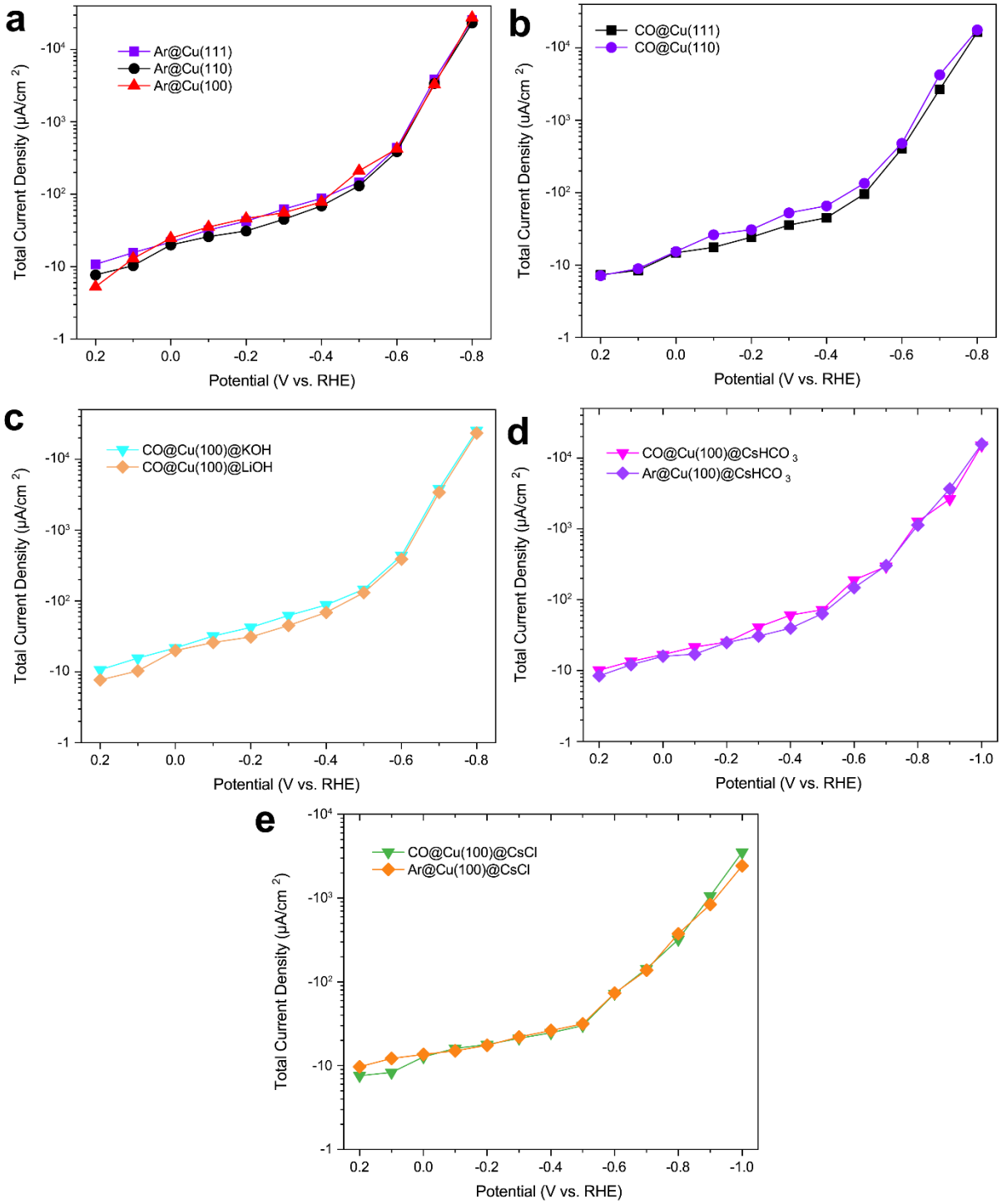

Figure S23 | The total current density for various Cu single-crystal surfaces under different conditions.

Table S4 | Electrochemical potentials of possible CO_2 reduction reactions in aqueous solutions for the production of different hydrocarbon fuels.(42)

Possible half-reactions of electrochemical CO_2 reduction	Electrode potentials (V vs. RHE) at pH=7	pH=13
CO_2 (g) + H_2O (l) + $2e^-$ → CO (g) + $2OH^-$	-0.10	0.06
CO_2 (g) + H_2O (l) + $2e^-$ → $HCOO^-$ (l) + OH^-	-0.03	0.13
CO_2 (g) + $5H_2O$ (l) + $6e^-$ → CH_3OH (l) + $6OH^-$	0.03	0.19
CO_2 (g) + $6H_2O$ (l) + $8e^-$ → CH_4 (g) + $8OH^-$	0.17	0.33
$2CO_2$ (g) + $8H_2O$ (l) + $12e^-$ → C_2H_4 (g) + $12OH^-$	0.08	0.24

Table S5 | Electrochemical potentials of possible CO reduction reactions in aqueous solutions for the production of different hydrocarbon fuels. The below half-reactions are obtained from equation addition or subtraction operations in Table S4.

Possible half-reactions of electrochemical CO reduction	Electrode potentials (V vs. RHE) at pH= 7	pH=13
CO (g) + $2OH^-$ -$2e^-$ → CO_2 (aq.) + H_2O (l)	0.10	0.26
CO (g) + OH^- → $HCOO^-$ (l)	0.07	0.23
CO (g) + $4H_2O$ (l) + $4e^-$ → CH_3OH (l) + $4OH^-$	0.13	0.29
CO (g) + $5H_2O$ (l) + $6e^-$ → CH_4 (g) + $6OH^-$	0.27	0.43
$2CO$ (g) + $6H_2O$ (l) + $8e^-$ → C_2H_4 (g) + $8OH^-$	0.18	0.34

2. Supporting Notes

Supporting Note 1 - the plasmon-enhanced effect in the SHINs/Cu nanogap

Compared to the situation at a plain Cu surface, the CORR and COOR would take place in a different environment within the hotspots. This is due to the fact that localized surface plasmon (LSP) resonances of metallic nanostructures will harvest and confine light near a metal surface via photon–electron interactions, leading to confined electromagnetic fields, charge transfer, local heat generation, as well as hot carrier excitation (43, 44). These LSP-induced phenomena within the hotspots could result in various effects in electrocatalytic reactions, e.g., field-induced reagent concentration (45), extreme nanophotonics and molecular optomechanics (46), anchoring group-based intermediates (47), strong dependence on the gap size (48), etc. However, it is hard to exclude these LSP-induced effects during the in-situ spectro-electro-chemical measurements. On the one hand, we can't record any useful Raman signals (e.g., adsorbed CO modes) of intermediates from the plain Cu(100) surface without SHINs (see Figure S8). On the other hand, the plasmon-enhanced effect in the nanogap can help to boost the Raman signals, and thus one can obtain some peaks during the SHINERS measurements (see Fig. 2).

Supporting Note 2 - isotope exchange effects for the ^{13}CO vs. ^{12}CO species

As shown in Figure 2a, the ^{13}CO isotopic substitution measurements were carried out on Cu(100) in the 0.1 M CsOH solution saturated with ^{13}CO. We found that the C≡O stretching vibrations at 2060 (on terrace sites) and 2090 cm^{-1} (on step sites) shift to lower wavenumbers around 2015 and 2045 cm^{-1} during the $^{13}CORR$, respectively. The ratio (γ) of the Raman frequency for $*CO_{atop}$ red-shift during the $^{13}CORR$ experiments can be approximately analyzed by the following reduced mass formula:(49, 50)

$$\gamma_1 = \frac{\nu(^{13}\mathrm{CO})}{\nu(^{12}\mathrm{CO})} = \frac{\sqrt{m(^{13}\mathrm{C}) + m(\mathrm{O})}}{\sqrt{m(^{13}\mathrm{C}) \times m(\mathrm{O})}} \Big/ \frac{\sqrt{m(^{12}\mathrm{C}) + m(\mathrm{O})}}{\sqrt{m(^{12}\mathrm{C}) \times m(\mathrm{O})}} = \frac{\sqrt{13+16}}{\sqrt{13\times16}} \Big/ \frac{\sqrt{12+16}}{\sqrt{12\times16}} = 97.8\%$$

Therefore, theoretically, the vibrational peaks at 2060 and 2090 cm^{-1} for $*CO_{atop}$ on Cu(100) should downward shift to around 2060 × 0.978 = 2015 and 2090 × 0.978 = 2044 cm^{-1} during the ^{13}CORR, respectively. This is in good agreement with our experimental observations (Figure 2a).

Supporting Note 3 – excluding possible overlaps from the $*HCO_3^-$/*COOH /$*CO_3^{2-}$ /$*CO_2^-$ species

To the best of our knowledge, both peaks at 1220 and 1370 cm^{-1} have not been previously observed on Cu surfaces during the $CO_{(2)}$RR in pH=13 electrolytes by SERS/SHINERS techniques. Due to the system complexity and co-existent pathways, the assignments of the 1220 and 1370 cm^{-1} bands may involve certain overlaps from other surface species. For example, Dunwell et al. observed IR peaks associated with $H^{12}CO_3^-$ (1362 cm^{-1}) and $H^{13}CO_3^-$ (1323 cm^{-1}) through ATR-IR spectrum deconvolution of the vibrational bands, which were recorded from Au films in $^{12/13}CO_2$-saturated $NaHCO_3$ electrolytes at pH=7.2 (31). These peak positions are pretty close to our observations, which might overlap the proposed assignments (-C=C- stretching) for the *HOCCOH species under ^{12}CO (1370 cm^{-1}) and ^{13}CO (1320 cm^{-1}) atmospheres (Fig. 2). Note that although in some cases one vibrational mode can be both IR (change in dipole moment) and Raman (change in polarizability) active, such a direct comparison between IR and Raman peaks needs to tread with care.

In order to exclude the possible spectral overlap, more EC-SHINERS spectra have been recorded on Cu(100) surface in 0.1 M Ar-saturated $CsHCO_3$ solutions (pH=9.0, Fig. S18b). At

the low overpotentials (+0.2 V to - 0.3 V, Fig. S18b), no significant Raman features can be observed around the 1220 and 1370 cm^{-1} regions in this electrolyte (dominated by $H^{12}CO_3^-$ anions), which presents direct evidence that they are not associated with $H^{12}CO_3^-$ adsorbed on Cu surfaces. At the same time, these two peaks appeared under lower potentials (-0.4 V to -1.0 V). This is due to the fact that the surface $H^{12}CO_3^-$ species will be reduced to CO (2085 cm^{-1}, Fig. S16b), and then the CORR occurs on Cu(100) to produce the *HOCCOH intermediates (Fig. S16b). Notably, it is well known that the $*HCO_3^-$ tends to deprotonate in pH=13 media (e.g., 0.1 M CsOH) and transform to the $*CO_3^{2-}$ species. For the same reason, although previous SERS (17) and ATR-SEIRAS (41) observations from Cu surfaces in CO_2-saturated $KHCO_3$ buffer (0.1M, pH=6.8) assigned the 1370 cm^{-1} peak to a carboxyl intermediate (*COOH), this assignment can not be applied to the current system due to the difference in electrolyte pH (Fig. 2, 0.1 M CsOH, pH=13.0).

Additionally, Chernyshova et al. reported that the co-existence of the 1350-1370 cm^{-1} peak with the peak at 1070 cm^{-1} could be associated with a typical symmetric C-O stretching of the CO_3^{2-} species (16). This overlap can be excluded from the D_2O labelling studies (Figs. 2a, c). Compared to the CORR in the CsOH electrolyte, the peak position at 1070 cm^{-1} remains unchanged while the 1370 cm^{-1} band slightly red-shifted to 1365 cm^{-1} in the CsOD electrolyte (Figs. 2a, c). On the contrary, the 1370 cm^{-1} band accompanied by the 1220 cm^{-1} band downward shifted to ca. 1365 and 1205 cm^{-1} simultaneously in the D_2O isotope experiments (Figs. 2a, c), indicating that both peaks are correlated with 'H' atoms (see Supporting Notes 3-5). Therefore, the 1370 cm^{-1} band accompanied by the 1070 cm^{-1} band should not be ascribed to the CO_3^{2-} species in our case. Moreover, Raman peaks at 350, 700, 1330, and 1540 cm^{-1} can be assigned to the $*CO_2^-$ (14, 16), which are beyond the regions around 1220 and 1370 cm^{-1} and thus the $*CO_2^-$ can also be excluded here.

Supporting Note 4- isotope exchange effects for ^{13}C-OH vs. ^{12}C-OH species

For the –C-OH related moiety during the ^{13}CORR, we found that the –C-OH stretching vibration at 1220 cm^{-1} shifts to lower wavenumbers around 1185 cm^{-1}. The ratio (γ) of the Raman frequency for –C-OH red-shift during the ^{13}CORR experiments can be approximately analyzed by the following mass formula:(49, 50)

$$\gamma_2 = \frac{\nu(^{13}\mathrm{COH})}{\nu(^{12}\mathrm{COH})} = \frac{\sqrt{m(^{13}\mathrm{C}) + m(\mathrm{OH})}}{\sqrt{m(^{13}\mathrm{C}) \times m(\mathrm{OH})}} \Big/ \frac{\sqrt{m(^{12}\mathrm{C}) + m(\mathrm{OH})}}{\sqrt{m(^{12}\mathrm{C}) \times m(\mathrm{OH})}} = \frac{\sqrt{13+17}}{\sqrt{13\times 17}} \Big/ \frac{\sqrt{12+17}}{\sqrt{12\times 17}} = 97.7\%$$

Therefore, theoretically, the vibrational peak at 1220 cm^{-1} for the –C-OH moiety should downward shift to around 1220 × 0.977 = 1192 cm^{-1} during the ^{13}CORR. This is in good agreement with our experimental observations (1185 cm^{-1}, Fig. 2a).

Supporting Note 5 - isotope exchange effects for the ^{12}C-OD vs. ^{12}C-OH species

For the –C-OH related moiety during the ^{12}CORR with D_2O as the electrolyte, we found that the –C-OH stretching vibration at 1220 cm^{-1} shifts to lower wavenumbers around 1205 cm^{-1}. The ratio (γ) of the Raman frequency for –C-OH red-shift during the ^{12}CORR experiments in the CsOD solution can be approximately analyzed by the following mass formula:(49, 50)

$$\gamma_3 = \frac{\nu(\mathrm{COD})}{\nu(\mathrm{COH})} = \frac{\sqrt{m(\mathrm{C}) + m(\mathrm{OD})}}{\sqrt{m(\mathrm{C}) \times m(\mathrm{OH})}} \Big/ \frac{\sqrt{m(\mathrm{C}) + m(\mathrm{OD})}}{\sqrt{m(\mathrm{C}) \times m(\mathrm{OH})}} = \frac{\sqrt{12+18}}{\sqrt{12\times 18}} \Big/ \frac{\sqrt{12+17}}{\sqrt{12\times 17}} = 98.8\%$$

Therefore, theoretically, the vibrational peak at 1220 cm^{-1} for the –C-OH moiety should downward shift to around 1220 × 0.988 = 1205 cm^{-1} in the deuterium experiments. This is in good agreement with our experimental observations (1205 cm^{-1}, Fig. 2a).

Supporting Note 6 - isotope exchange effects for the –^{13}C=^{13}C- vs. –^{12}C=^{12}C- species

For the –C=C- related moiety during the ^{13}CORR, we found that the –C=C- stretching vibration at 1370 cm^{-1} shifts to lower wavenumbers around 1320 cm^{-1}. The ratio (γ) of the Raman frequency for –C=C- red-shift during the ^{13}CORR experiments can be approximately analyzed by the following mass formula:(49, 50)

$$\gamma_4 = \frac{\nu(^{13}C^{13}C)}{\nu(^{12}C^{12}C)} = \frac{\sqrt{m(^{13}C) + m(^{13}C)}}{\sqrt{m(^{13}C) \times m(^{13}C)}} \Big/ \frac{\sqrt{m(^{12}C) + m(^{12}C)}}{\sqrt{m(^{12}C) \times m(^{12}C)}} = \frac{\sqrt{13+13}}{\sqrt{13\times 13}} \Big/ \frac{\sqrt{12+12}}{\sqrt{12\times 12}} = 96.0\%$$

Therefore, theoretically, the vibrational peak at 1370 cm^{-1} for the –C=C- moiety should downward shift to around 1370 × 0.96 = 1315 cm^{-1} during the ^{13}CORR. This is in good agreement with our experimental observations (1320 cm^{-1}, Fig. 2a).

Supporting Note 7 – AIMD calculations for the *CO_2^- species on Cu(100) and Cu(111)

Under a vacuum condition, molecular CO_2 can physically adsorb on the Cu surface in both Cu (100) and Cu (111) facets (28). However, the CO_2^- species is unstable on the Cu surfaces in the vacuum and can only be stabilized in the aqueous condition during ab-initio molecular dynamics calculations. To understand the vibration fingerprints of CO_2^- species, we simulated the CO_2^- species that chemically adsorbed on Cu(100) and Cu(111) with explicit solvation. The chemically adsorbed CO_2 is bent and more negatively charged (by 0.45 |e| according to the Mulliken charge population) compared to the physically absorbed CO_2 species. The vibrational frequencies differ between two Cu surfaces (Fig. 3b). On the one hand, the AIMD calculations of the CO_2^- species on Cu(100) indicate vibrational frequencies at 725, 1105 and 1345 cm^{-1} (**Table S3**), which are in good agreement with Cheng's calculated VDOSs (28). On the other hand, the AIMD results indicate vibrational frequencies at 680, 1103, and 1535-1604 cm^{-1} on Cu(111) (**Table S3**).

Based on the isotopic experiments and DFT calculations as reported by Chernyshova et al. (16), the vibrational frequencies of chemically adsorbed CO_2^- species have been determined to be around 703 (in-plan bending), 1330 (symmetry stretching), and 1520-1540 cm^{-1} (asymmetry stretching). Note that their simulations were carried out at Cu(111) surface using a static vibrational analysis, which only successfully predicted the bending mode (733 cm^{-1}) and asymmetry stretching (1503 cm^{-1}) of the CO_2^- species (16). The symmetry stretching mode at 1330 cm^{-1} in the experimental result was far away from the DFT prediction (at 967 cm^{-1}) (16). To understand this discrepancy, we carried out AIMD simulations on CO_2 adsorbed both on Cu(100) and Cu(111) (**Table S3**). It is evident that our AIMD simulations can reproduce the frequency regions at 1345 cm^{-1} on Cu(100) and 1535-1604 cm^{-1} on Cu(111). We proposed that these peaks were associated with the asymmetry stretching modes of the CO_2^- species on different Cu facets (**Table S3**). This assumption can also be backed up by several experimental facts that even Cu single-crystal facets tend to reconstruct quickly under $CO_{(2)}$ reduction conditions (21, 51, 52). Thus the CO oxidation occurs both on Cu(100) and Cu(111) simultaneously. While, the similar calculated frequencies around 700 (725 on Cu(100)/680 on Cu(111)) and 1100 (1105 Cu(100)/1103 Cu(111)) cm^{-1} both on Cu(100)/Cu(111) would be associated with their symmetry stretching modes and in-plane bending modes, respectively (**Table S3**). Interestingly, the *HCOO species (with two oxygen bound with Cu sites) also present peaks around 1506 cm^{-1} on Cu(100) surface, which might contribute to the Raman signals as observed from our experiments in the $CsHCO_3$ (Fig. S18) and CsCl (Fig. S19) solutions.

Supporting Note 8 - isotope exchange effects for the *OD vs. *OH species

For the *OH species on Cu(100) during the ^{12}CORR with D_2O as the electrolyte, we found that *OH bending vibration at 538 cm^{-1} shifts to lower wavenumbers 530 cm^{-1} at 0.4 V (vs. RHE). The ratio (γ) of the Raman frequency for *OH downward shift in the CORR in CsOD experiments can be approximately analyzed by the following mass formula:

$$\gamma_7 = \frac{\nu(\mathrm{OD})}{\nu(\mathrm{OH})} = \frac{\sqrt{m(\mathrm{O}) + m(\mathrm{D})}}{\sqrt{m(\mathrm{O}) \times m(\mathrm{D})}} \Big/ \frac{\sqrt{m(\mathrm{O}) + m(\mathrm{H})}}{\sqrt{m(\mathrm{O}) \times m(\mathrm{H})}} = \frac{\sqrt{16+2}}{\sqrt{16\times 2}} \Big/ \frac{\sqrt{16+1}}{\sqrt{12\times 1}} = 72.8\%$$

Therefore, theoretically, the vibrational peak at 538 cm^{-1} for the *OH species should downward shift to around 530 × 0.728 = 392 cm^{-1} in the deuterium experiment. However, in actual experimental research systems, the hydrogen bonding with electrolyte molecules and the interaction with surface *D_2O/*O species may become more pronounced for the *OH/*OD in higher alkaline solutions (pH=13).(10) Thus, it should not exhibit a significant isotopic shift in actual D_2O experiments compared with the calculation result without taking those factors as mentioned above into consideration.

Supporting Note 9 – calculations for the co-adsorbed *OH/*O and *CO species

Due to the high cost, it is challenging to include all surface states (e.g., *OH/*O or $CuO_x/(OH)_y$ species) on Cu(100) together during ab-initio molecular dynamics simulations, although the coupling between *OH/*O and C-containing adsorbates exist. (24, 53) The surface *O and *OH species may contribute to the reaction reactivity/selectivity of the $CO_{(2)}$RR and the vibrational modes of the intermediates since they could react with the surface C-containing intermediates or water molecules. This will give rise to different reaction products via various intermediaries. However, according to several benchmark simulations, the *CO model adsorbed on clean Cu(100) contains quite similar vibrational modes as that obtained from the *CO+*O(Θ = 0.25) and *CO+*OH(Θ = 0.25) models (see Fig. S24). The difference in their

VDOS intensities is probably due to the occupation of active sites by the *OH/*O and the interaction between the *CO and *OH/*O on Cu(100). (24, 53) More detailed and comprehensive simulations are indeed essential to fully understand the $CO_{(2)}$RR on the Cu surface but beyond the current computational affordability.

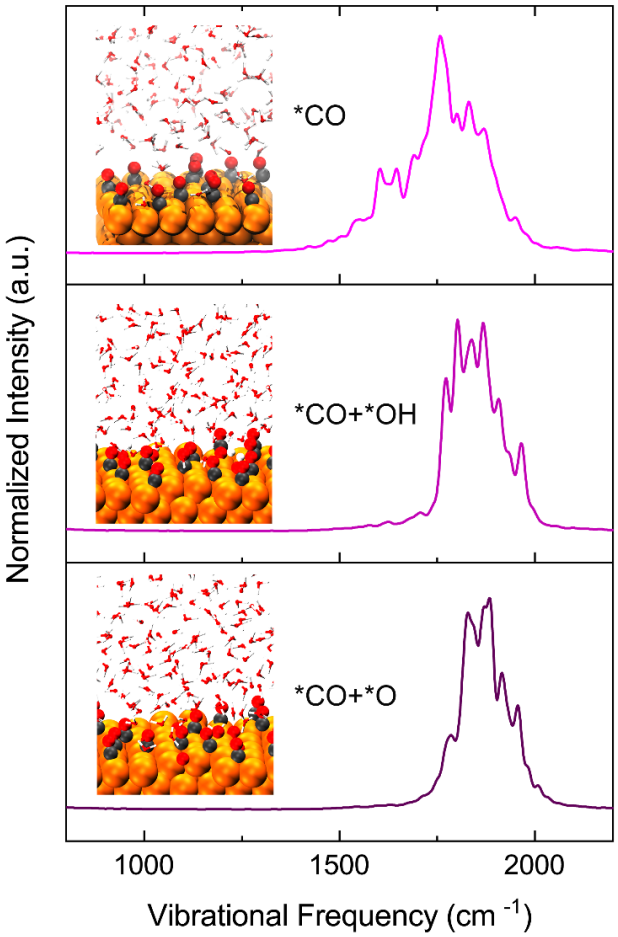

Figure S24 | VDOSs as obtained from AIMD simulations and representative snapshots of typical *CO and its co-adsorbed *OH/*O intermediates on Cu(100). The surface coverage (Θ) of the *CO model was set at 1/3 monolayer (ML). The *CO model adsorbed on clean Cu(100) contains quite similar vibrational modes as that obtained from the *CO+*O (Θ = 1/4 ML) and *CO+*OH (Θ = 1/4 ML) models. The difference in their relative intensities is probably due to the occupation of active sites by the *OH/*O and the interaction between the *CO and *OH/*O on Cu(100).(24, 53) The Cu, C, O, and H atoms are presented in orange, black, red, and white colours, respectively. a.u. arbitrary units.

Supporting Note 10 – calculations with and without the cation effect and potential bias

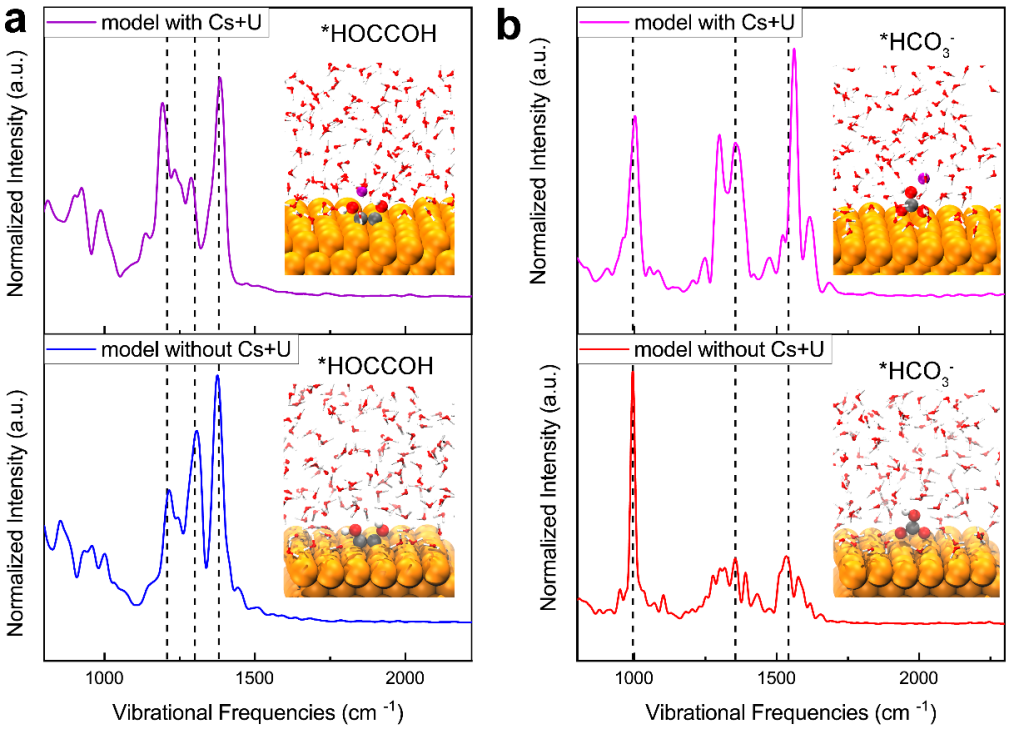

Figure S25 | VDOSs as obtained from AIMD simulations and representative snapshots of typical (a) *HOCCOH and (b) $*HCO_3^-$ species on Cu(100) with and without the cation effect (Cs^+) and potential bias (U). The Cu(100) electric double layers of the models with Cs+U include a Cs^+ ion and 132 explicit water molecules, and the corresponding surface charge densities are -6.81 μC/cm^2. The Cs, Cu, C, O, and H atoms are presented in purple, orange, black, red, and white colours, respectively. a.u. arbitrary units.

Due to the high cost, it is challenging to consider all cation effects and potential bias together during our ab-initio molecular dynamics simulations for all intermediates, although these factors will induce shifts of vibrational frequencies under certain conditions. (27, 40) However, our in-situ EC-SHINERS spectra mostly obtained from Cu surfaces under low applied potentials (+0.2 to -0.5 V vs. RHE) and current densities (ca. > -100 μA/cm^2, see Fig. 2), which mild conditions render us to take simplified simulation models to save computation time and

sources. To provide more reliable comparisons, we carried out additional AIMD simulations, which included Cs^+ cations and applied potentials in the models. Based on the calculation results (Fig. S25), these vibrational frequencies of typical intermediates (e.g., *HOCCOH and $*HCO_3^-$) are pretty similar for both models with and without cation (Cs^+) and potential (U) conditions. In addition, the difference in their VDOS intensities doesn't affect the assignments of the corresponding surface species. More detailed and comprehensive simulations are indeed essential to fully understand the $CO_{(2)}$RR on the Cu surface but beyond the current computational affordability.

3. Supporting Methods

3.1. Chemicals and Materials

Cesium hydroxide monohydrate (99.95% trace metals basis), potassium hydroxide (99.99% trace metals basis), lithium hydroxide monohydrate (99.995% trace metals basis), cesium hydrogencarbonate (99.9%), cesium chloride (99.999% trace metals basis), perchloric acid (70%), sulfuric acid (96%), phosphoric acid solution (85% in water, 99.94% metals basis), potassium phosphate dibasic trihydrate (99%), potassium phosphate monobasic (99%) and sodium perchlorate (≥98.0%) were purchased from Sigma-Aldrich. Deuterium oxide (99.9 atom % D) and ^{13}CO isotopic gas (99 atom % ^{13}C) were purchased from Cambridge Isotope Laboratories, Inc. All chemicals were used as received. Argon (99.999%) and nitrogen (99.999%) were purchased from Chem-Gas Pte Ltd. Carbon monoxide (99.97%) was purchased from Linde Gas Singapore Pte Ltd. Deionized water (18.2 MΩ·cm, Barnstead Type 1) was used for all the studies. Shell-isolated nanoparticles (SHINs) were donated by Prof.

Jian-Feng Li's group (Xiamen University, China), prepared using previously-reported protocols.(54)

3.2. Pretreatment of Cu single-crystal and polycrystalline electrodes

Cu(100), Cu(111), and Cu(110) single-crystal discs (99.999%, GoodFellow, 10 mm in diameter and 2 mm in thickness) were used as working electrodes and were prepared based on our previous-reported protocols.(55) Briefly, the Cu single-crystal surfaces were gently polished with nano-diamond slurries (DiaPro Nap ¼ μm, Struers) to mirror-like finishes, and then electropolished in an acidic electrolyte at +2 A/cm^2 for 1 second (Autolab PGSTAT100). The electropolishing acidic solution was prepared by mixing 130 mL H_3PO_4 (85% in water, Sigma-Aldrich, 99.94% metals basis), 20 mL H_2SO_4 (96% in water, Sigma-Aldrich), and 60 mL deionized water (18.2 MΩ·cm). Immediately afterward, the single-crystal discs were rinsed with deionized water and 0.1 mM $HClO_4$ solution (Sigma-Aldrich). The surface structures of the single-crystal electrodes were checked using cyclic voltammetry (CV) in N_2-purged 0.1 M KOH (Sigma-Aldrich, 99.99% trace metals basis), at 50 mV/s between -0.45 V and +0.45 V vs. RHE.

The polycrystalline Cu (polyCu) discs (99.99%, Goodfellow) were first mechanically polished with SiC paper (grit 1200, Struers) and diamond slurries (Diapro, 9 μm and 3 μm, Struers) to a mirror-like finish, then sonicated and rinsed with deionized water. In order to gain a strong surface-enhanced Raman scattering (SERS) effect, the polyCu electrodes were then electrochemically roughened by a square wave potential pulses (SWPP) method (56). The morphology of the polyCu electrodes was characterized by SEM imaging (JEOL JSM-6710F).

3.3. FDTD calculations

The spatial distribution and absorption spectra of local electric fields in the nanogaps between a Cu surface and a 2 × 2 array of Au@SiO_2 SHINs were calculated using the FDTD method (Lumerical Solution). The simulation model comprised four Au@SiO_2 SHINs (the diameter of the Au core is ca. 55 nm and the thickness of the SiO_2 shell is ca. 3 nm, Fig. S2) and a Cu metal slab. The incident wavelength is set at 633 nm. In the simulation, a perfectly matched layer was used. The simulation time was set to 1000 fs, which was enough to ensure convergence of the calculation. We adopted a non-uniform mesh size in the junctions of the investigated structures. The Yee cell size in the junctions of the particle–particle and particle–Cu film was 0.25 nm× 0.25 nm× 0.25 nm and for the remaining regions was 0.5 nm× 0.5 nm× 0.5 nm. The dielectric functions of Cu and Au, which are wavelength-dependent, were taken from a multi-coefficient fitting model offered by Lumerical FDTD (50).

3.4. Spectral processing

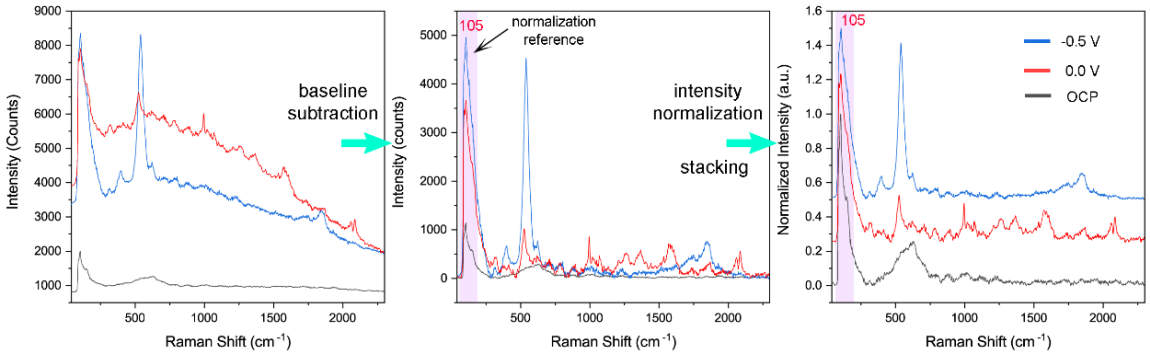

Figure S26 | Normalization processing of typical averaged spectra under different conditions (Fig. 2a). OCP: open circuit potential. All potentials are referenced to the reversible hydrogen electrode (RHE). a.u. arbitrary units.

All in-situ SHINERS spectra were acquired from at least three different spots with three repeats each. Each presented spectrum is an average of acquired spectra with a collection time of 20 seconds each. These averaged spectra are reported without smoothing. To make all spectra comparable, they are normalized to the intensity of the low-frequency band at 105 cm^{-1}, which is characteristic of the optical fibers used in our spectrometer and it is always the highest peak as the internal standard during the measurements. The background was subtracted by using the baseline correction function (Type: Lines, Degree: 5), and the peak position was determined by using the add peak function in the LabSpec 5 Spectral Software Suite (build-in software in the HORIBA system). The arbitrary scaling of the spectra is set as 1 unit (at the 105 cm^{-1} band), and then they are stacked (shift up 0.25 units each time) in the Origin (OriginLab, 2019b) for better clarification.

3.5. DFT and AIMD computational details

(i) vibrational analysis based on DFT calculations

The theoretical prediction of vibrational spectra is a well-established field of computational chemistry. The commonly used approach is based on the harmonic approximation, where the modes are assumed to be harmonic oscillators. The stationary point of the oscillator is obtained from the geometry optimization, and the frequencies are derived from the second derivatives of the energy.

The gradient of the potential energy surface is determined via the finite differences method.

$$D_{ij} = \frac{\partial^2 E}{\partial R_i \, \partial R_j}$$

Where $\boldsymbol{E}$ is the potential energy, $\boldsymbol{R}$ is the position. The force constant matrix $\boldsymbol{D_{ij}}$(Hessian) is then diagonalized to yield the eigenvectors and eigenvalues.

Although static vibrational analysis has been proved to work in many cases, it neglects the anharmonicity and thermal effect. Another issue for the static calculation is that the influence of the solvent cannot be considered due to its dynamical nature, although continuum solvation models can simulate the electrostatic environment. However, the interaction of the solvent molecules is known to be non-negligible in many cases, especially when the hydrogen bond is involved between the solvent and target molecule/group. Therefore, it is necessary to explicitly consider the solvent molecules as well as their dynamic nature using a molecular dynamics approach.

(ii) computational workflow of AIMD simulations

We first prepared the surface intermediates by optimizing their geometries adsorbed on Cu(100). The structures were first optimized using static DFT calculations (see Fig. S27a). The vibrational analysis was based on the optimized geometry and summarized in Supporting Tables 2 and 3. Starting from the optimized geometry, we further included explicit solvent molecules in the system and ran AIMD simulations. The water film was added and equilibrated for about 5 ps, keeping the intermediates and Cu surface fixed. (see Fig. S27b) The production runs were about 10 ps for each intermediate, keeping the intermediates and Cu surface relaxed (see Fig. S27c).

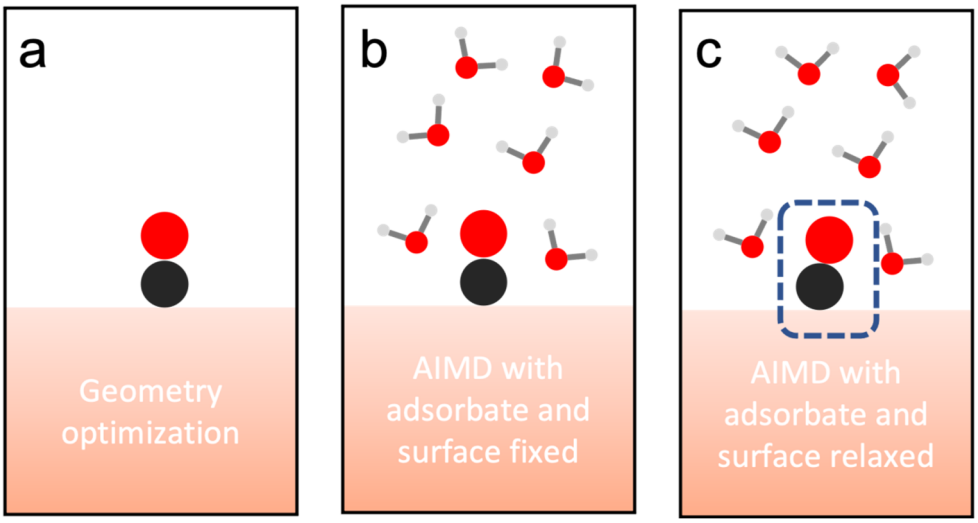

Figure S27 | Computational workflow of the ab-initio molecular dynamics simulations. (a) Geometry optimization of the adsorbate and surface, where the optimized geometry is used for vibrational analysis based on the finite difference method; (b) Pre-equilibrium of the AIMD simulations with explicit water molecules where the adsorbate and surface are kept fixed; (c) AIMD simulations with adsorbate and surface relaxed. As illustrated in the box, the trajectory of adsorbates is used to calculate the vibrational density of states. Color code: The slab of Cu is orange; the adsorbate (CO as an example) is black (carbon) and red (oxygen); hydrogen is grey.

4. Supporting Videos

Movie S1. AIMD simulation of the protonation process from the *OCCO to *OCCOH and *HOCCOH species at the aqueous/Cu(100) interface. The Cu, C, O, and H atoms are presented in orange, black, red, and white colours, respectively. The reacted surface H2O molecules are presented in green colour.

Movie S2. AIMD simulation of the protonation process from the *OCCOH to *HOCCOH species at the aqueous/Cu(100) interface. The Cu, C, O, and H atoms are presented in orange, black, red, and white colours, respectively. The reacted surface H2O molecules are presented in green colour.

5. Supporting References

1. N. Bodappa *et al.*, Early Stages of Electrochemical Oxidation of Cu(111) and Polycrystalline Cu Surfaces Revealed by in Situ Raman Spectroscopy. *J. Am. Chem. Soc.* **141**, 12192-12196 (2019).
2. H. Y. H. Chan, C. G. Takoudis, M. J. Weaver, Oxide Film Formation and Oxygen Adsorption on Copper in Aqueous Media As Probed by Surface-Enhanced Raman Spectroscopy. *J. Phys. Chem. B* **103**, 357-365 (1999).
3. Y. Deng, A. D. Handoko, Y. Du, S. Xi, B. S. Yeo, In Situ Raman Spectroscopy of Copper and Copper Oxide Surfaces during Electrochemical Oxygen Evolution Reaction: Identification of CuIII Oxides as Catalytically Active Species. *ACS Catal.* **6**, 2473-2481 (2016).
4. A. Singhal *et al.*, Copper(I) Oxide Nanocrystals – One Step Synthesis, Characterization, Formation Mechanism, and Photocatalytic Properties. *Eur. J. Inorg. Chem.* **2013**, 2640-2651 (2013).
5. L. Debbichi, M. C. Marco de Lucas, J. F. Pierson, P. Krüger, Vibrational Properties of CuO and Cu4O3 from First-Principles Calculations, and Raman and Infrared Spectroscopy. *J. Phys. Chem. C* **116**, 10232-10237 (2012).
6. W. Wang *et al.*, A simple wet-chemical synthesis and characterization of CuO nanorods. *Appl. Phys. A* **76**, 417-420 (2003).
7. D. Kang *et al.*, Oxidation Resistance of Iron and Copper Foils Coated with Reduced Graphene Oxide Multilayers. *ACS Nano* **6**, 7763-7769 (2012).
8. J. C. Hamilton, J. C. Farmer, R. J. Anderson, In Situ Raman Spectroscopy of Anodic Films Formed on Copper and Silver in Sodium Hydroxide Solution. *J. Electrochem. Soc.* **133**, 739-745 (1986).
9. M. He *et al.*, Oxygen induced promotion of electrochemical reduction of CO2 via co-electrolysis. *Nat. Commun.* **11**, 3844 (2020).
10. Y. Zhao *et al.*, Speciation of Cu Surfaces During the Electrochemical CO Reduction Reaction. *J. Am. Chem. Soc.* **142**, 9735-9743 (2020).
11. G. Niaura, Surface-enhanced Raman spectroscopic observation of two kinds of adsorbed OH− ions at copper electrode. *Electrochim. Acta* **45**, 3507-3519 (2000).
12. Y. Yang *et al.*, Insight into the Formation and Transfer Process of the First Intermediate of CO2 Reduction over Ag-Decorated Dendritic Cu. *Chem. Eur. J.* **26**, 4080-4089 (2020).
13. S. Härtinger, B. Pettinger, K. Doblhofer, Cathodic formation of a hydroxyde adsorbate on copper (111) electrodes in alkaline electrolyte. *J. Electroanal. Chem.* **397**, 335-338 (1995).
14. M. Moradzaman, G. Mul, In Situ Raman Study of Potential-Dependent Surface Adsorbed Carbonate, CO, OH, and C Species on Cu Electrodes During Electrochemical Reduction of CO2. *ChemElectroChem* **8**, 1478-1485 (2021).
15. F. Li *et al.*, Molecular tuning of CO2-to-ethylene conversion. *Nature* **577**, 509-513 (2020).
16. I. V. Chernyshova, P. Somasundaran, S. Ponnurangam, On the origin of the elusive first intermediate of CO2 electroreduction. *Proc. Natl. Acad. Sci. U. S. A.* **115**, E9261-E9270 (2018).
17. S. Jiang, K. Klingan, C. Pasquini, H. Dau, New aspects of operando Raman spectroscopy applied to electrochemical CO2 reduction on Cu foams. *J. Chem. Phys.* **150**, 041718 (2018).
18. N. Heidary, K. H. Ly, N. Kornienko, Probing CO2 Conversion Chemistry on Nanostructured Surfaces with Operando Vibrational Spectroscopy. *Nano Letters* **19**, 4817-4826 (2019).
19. I. Mrozek, C. Pettenkofer, A. Otto, Raman spectroscopy of carbon monoxide adsorbed on silver island films. *Surf. Sci.* **238**, 192-198 (1990).
20. Y. Deng, B. S. Yeo, Characterization of Electrocatalytic Water Splitting and CO2 Reduction Reactions Using In Situ/Operando Raman Spectroscopy. *ACS Catal.* **7**, 7873-7889 (2017).
21. C. M. Gunathunge *et al.*, Spectroscopic Observation of Reversible Surface Reconstruction of Copper Electrodes under CO2 Reduction. *J. Phys. Chem. C* **121**, 12337-12344 (2017).
22. A. S. Malkani, M. Dunwell, B. Xu, Operando Spectroscopic Investigations of Copper and Oxide-Derived Copper Catalysts for Electrochemical CO Reduction. *ACS Catal.* **9**, 474-478 (2019).

23. P. Hollins, The influence of surface defects on the infrared spectra of adsorbed species. *Surf. Sci. Rep.* **16**, 51-94 (1992).
24. X. Chang, Y. Zhao, B. Xu, pH Dependence of Cu Surface Speciation in the Electrochemical CO Reduction Reaction. *ACS Catal.* **10**, 13737-13747 (2020).
25. E. Pérez-Gallent, M. C. Figueiredo, F. Calle-Vallejo, M. T. M. Koper, Spectroscopic Observation of a Hydrogenated CO Dimer Intermediate During CO Reduction on Cu(100) Electrodes. *Angew. Chem. Int. Ed.* **56**, 3621-3624 (2017).
26. Y. Kim *et al.*, Time-resolved observation of C–C coupling intermediates on Cu electrodes for selective electrochemical CO2 reduction. *Energy Environ. Sci.* **13**, 4301-4311 (2020).
27. T. Cheng, A. Fortunelli, W. A. Goddard, Reaction intermediates during operando electrocatalysis identified from full solvent quantum mechanics molecular dynamics. *Proc. Natl. Acad. Sci. U. S. A.* **116**, 7718 (2019).
28. T. Cheng, A. Fortunelli, W. A. Goddard, Reaction intermediates during operando electrocatalysis identified from full solvent quantum mechanics molecular dynamics. *Proc. Natl. Acad. Sci. U. S. A.* **116**, 7718-7722 (2019).
29. K. Klingan *et al.*, Reactivity Determinants in Electrodeposited Cu Foams for Electrochemical CO2 Reduction. *ChemSusChem* **11**, 3449-3459 (2018).
30. Y.-Y. Yang *et al.*, Infrared Spectroelectrochemical Study of Dissociation and Oxidation of Methanol at a Palladium Electrode in Alkaline Solution. *Langmuir* **29**, 1709-1716 (2013).
31. M. Dunwell *et al.*, The Central Role of Bicarbonate in the Electrochemical Reduction of Carbon Dioxide on Gold. *J. Am. Chem. Soc.* **139**, 3774-3783 (2017).
32. L. Wang, K. Gupta, J. B. M. Goodall, J. A. Darr, K. B. Holt, In situ spectroscopic monitoring of CO2 reduction at copper oxide electrode. *Faraday Discuss.* **197**, 517-532 (2017).
33. F. Milella, M. Mazzotti, Estimating speciation of aqueous ammonia solutions of ammonium bicarbonate: application of least squares methods to infrared spectra. *React. Chem. Eng.* **4**, 1284-1302 (2019).
34. H. An *et al.*, Sub-Second Time-Resolved Surface-Enhanced Raman Spectroscopy Reveals Dynamic CO Intermediates during Electrochemical CO2 Reduction on Copper. *Angew. Chem. Int. Ed.* **60**, 16576-16584 (2021).
35. T. Cheng, H. Xiao, W. A. Goddard, Full atomistic reaction mechanism with kinetics for CO reduction on Cu(100) from ab initio molecular dynamics free-energy calculations at 298 K. *Proc. Natl. Acad. Sci. U. S. A.* **114**, 1795 (2017).
36. W. Luc *et al.*, Two-dimensional copper nanosheets for electrochemical reduction of carbon monoxide to acetate. *Nat. Catal.* **2**, 423-430 (2019).
37. H.-Y. Chen, M.-H. Lin, C.-Y. Wang, Y.-M. Chang, S. Gwo, Large-scale hot spot engineering for quantitative SERS at the single-molecule scale. *J. Am. Chem. Soc.* **137**, 13698-13705 (2015).
38. J.-F. Li *et al.*, Electrochemical shell-isolated nanoparticle-enhanced Raman spectroscopy: correlating structural information and adsorption processes of pyridine at the Au (hkl) single crystal/solution interface. *J. Am. Chem. Soc.* **137**, 2400-2408 (2015).
39. H. Tian, N. Zhang, L. Tong, J. Zhang, In Situ Quantitative Graphene-Based Surface-Enhanced Raman Spectroscopy. *Small Methods* **1**, 1700126 (2017).
40. C.-Y. Li *et al.*, In situ probing electrified interfacial water structures at atomically flat surfaces. *Nat. Mater.* **18**, 697-701 (2019).
41. S. Zhu, B. Jiang, W.-B. Cai, M. Shao, Direct Observation on Reaction Intermediates and the Role of Bicarbonate Anions in CO2 Electrochemical Reduction Reaction on Cu Surfaces. *J. Am. Chem. Soc.* **139**, 15664-15667 (2017).
42. K. P. Kuhl *et al.*, Electrocatalytic Conversion of Carbon Dioxide to Methane and Methanol on Transition Metal Surfaces. *J. Am. Chem. Soc.* **136**, 14107-14113 (2014).
43. C. Zhan *et al.*, From plasmon-enhanced molecular spectroscopy to plasmon-mediated chemical reactions. *Nat. Rev. Chem.* **2**, 216-230 (2018).
44. F. Shao *et al.*, In-situ nanospectroscopic imaging of plasmon-induced two-dimensional [4+4]-cycloaddition polymerization on Au(111). *Nat. Commun.* **12**, 4557 (2021).
45. M. Liu *et al.*, Enhanced electrocatalytic CO2 reduction via field-induced reagent concentration. *Nature* **537**, 382-386 (2016).

46. J. J. Baumberg, J. Aizpurua, M. H. Mikkelsen, D. R. Smith, Extreme nanophotonics from ultrathin metallic gaps. *Nat. Mater.* **18**, 668-678 (2019).
47. D. Wright *et al.*, Mechanistic study of an immobilized molecular electrocatalyst by in situ gap-plasmon-assisted spectro-electrochemistry. *Nat. Catal.* **4**, 157-163 (2021).
48. M. L. Pedano, S. Li, G. C. Schatz, C. A. Mirkin, Periodic Electric Field Enhancement Along Gold Rods with Nanogaps. *Angew. Chem. Int. Ed.* **49**, 78-82 (2010).
49. J. M. Rodgers *et al.*, Kinetic Isotope Effect Provides Insight into the Vibrational Relaxation Mechanism of Aromatic Molecules: Application to Cyano-phenylalanine. *J. Phys. Chem. Lett.* **7**, 1281-1287 (2016).
50. J.-C. Dong *et al.*, In situ Raman spectroscopic evidence for oxygen reduction reaction intermediates at platinum single-crystal surfaces. *Nat. Energy* **4**, 60-67 (2019).
51. F. Scholten, K.-L. C. Nguyen, J. P. Bruce, M. Heyde, B. Roldan Cuenya, Identifying Structure–Selectivity Correlations in the Electrochemical Reduction of CO2: A Comparison of Well-Ordered Atomically Clean and Chemically Etched Copper Single-Crystal Surfaces. *Angew. Chem. Int. Ed.* **60**, 19169-19175 (2021).
52. Y.-G. Kim *et al.*, Surface reconstruction of pure-Cu single-crystal electrodes under CO-reduction potentials in alkaline solutions: A study by seriatim ECSTM-DEMS. *J. Electroanal. Chem.* **780**, 290-295 (2016).
53. P. Farinazzo Bergamo Dias Martins *et al.*, Hydrogen evolution reaction on copper: Promoting water dissociation by tuning the surface oxophilicity. *Electrochem. Commun.* **100**, 30-33 (2019).
54. J. F. Li *et al.*, Shell-isolated nanoparticle-enhanced Raman spectroscopy. *Nature* **464**, 392-395 (2010).
55. Y. Huang, A. D. Handoko, P. Hirunsit, B. S. Yeo, Electrochemical Reduction of CO2 Using Copper Single-Crystal Surfaces: Effects of CO* Coverage on the Selective Formation of Ethylene. *ACS Catal.* **7**, 1749-1756 (2017).
56. M. Guo *et al.*, Rapid fabrication of SERS substrate and superhydrophobic surface with different micro/nano-structures by electrochemical shaping of smooth Cu surface. *Appl. Surf. Sci.* **353**, 1277-1284 (2015).